

1 **Decreasing trends of ammonia emissions over Europe seen
2 from remote sensing and inverse modelling**

3

4 **Ondřej Tichý¹, Sabine Eckhardt², Yves Balkanski³, Didier Hauglustaine³,
5 Nikolaos Evangelou^{2,*}**

6

7 ¹ The Czech Academy of Sciences, Institute of Information Theory and Automation, Prague,
8 Czech Republic.

9 ² ~~The Climate and Environmental Research Institute~~ NILU, Department of Atmospheric and
10 Climate Research (ATMOS), Kjeller, Norway.

11 ³ Laboratoire des Sciences du Climat et de l'Environnement (LSCE), CEA-CNRS-UVSQ,
12 91191, Gif-sur-Yvette, France.

13

14 * Corresponding author: N. Evangelou (Nikolaos.Evangelou@nilu.no)

15

Deleted: Norwegian Institute for Air Research ()
Deleted:)

18 **Abstract**

19 Ammonia (NH₃), a significant precursor of particulate matter, not only affects
20 biodiversity, ecosystems, soil acidification, but also climate and human health. In addition, its
21 concentrations are constantly rising due to increasing feeding needs and the large use of
22 fertilization and animal farming. Despite the significance of ammonia, its emissions are
23 associated with large uncertainties, while its atmospheric abundance is difficult to measure.
24 Nowadays, satellite products can effectively measure ammonia with low uncertainty and a
25 global coverage. Here, we use satellite observations of column ammonia in combination with
26 an inversion algorithm to derive ammonia emissions with a high resolution over Europe for the
27 period 2013–2020. Ammonia emissions peak in Northern Europe, due to agricultural
28 application and livestock management, in Western Europe (industrial activity) and over Spain
29 (pig farming). Emissions have decreased by -26% since 2013 (from 5431 Gg in 2013 to 3994
30 Gg in 2020) showing that the abatement strategies adopted by the European Union have been
31 very efficient. The slight increase (+4.4%) in 2015 is also reproduced here and is attributed to
32 some European countries exceeding annual emission targets. Ammonia emissions are low in
33 winter (286 Gg) and peak in summer (563 Gg) and are dominated by the temperature dependent
34 volatilization of ammonia from the soil. The largest emission decreases were observed in
35 Central and Eastern Europe (-38%) and in Western Europe (-37%), while smaller decreases
36 were recorded in Northern (-17%) and Southern Europe (-7.6%). When complemented against
37 ground observations, modelled concentrations using the posterior emissions showed improved
38 statistics, also following the observed seasonal trends. The posterior emissions presented here
39 also agree well with respective estimates reported in the literature and inferred from bottom-up
40 and top-down methodologies. These results indicate that satellite measurements combined with
41 inverse algorithms constitute a robust tool for emission estimates and can infer the evolution of
42 ammonia emissions over large timescales.

43

44 **1 Introduction**

45 Ammonia (NH_3), the only alkaline gas in the atmosphere, constitutes one of the most
46 reactive nitrogen species. It is produced from decomposition of urea, which is a rapid process
47 when catalyzed by enzymes (Sigurdarson et al., 2018). The main sectors contributing to its
48 production are livestock management and wild animals (Behera et al., 2013), biomass burning
49 and domestic coal combustion (Fowler et al., 2004; Sutton et al., 2008), volcanic eruptions
50 (Sutton et al., 2008), and agriculture (Erisman et al., 2007). Emissions from agricultural activity
51 and livestock management represent over 80% of the total emissions (Crippa et al., 2020), while
52 their regional contribution can reach 94% (Van Damme et al., 2018).

53 Once emitted, it is transported over short distances and deposited to water bodies, soil or
54 vegetation with a typical atmospheric lifetime of a few hours (Evangelou et al., 2021). It can
55 then lead to eutrophication of water bodies (Stevens et al., 2010), modulate soil pH (Galloway
56 et al., 2003) and «burn» vegetation by pulling water from the leaves (Krupa, 2003). It also reacts
57 with the abundant atmospheric sulfuric and nitric acids (Malm, 2004) forming fine particulate
58 matter (PM2.5) (Tsimpidi et al., 2007). While ammonia has a short atmospheric lifetime, PM2.5
59 resides significantly longer in the atmosphere, on the order of days to weeks (Seinfeld and
60 Pandis, 2000), and hence is transported over longer distances. Accordingly, secondary PM2.5
61 can affect the Earth's radiative balance, both directly by scattering incoming radiation (Henze
62 et al., 2012) and indirectly as cloud condensation nuclei (Abbatt et al., 2006). Its environmental
63 effects include visibility problems and contribution to haze formation. Finally, PM2.5 affects
64 human health, as it penetrates the human respiratory system and deposits in the lungs and
65 alveolar regions (Pope and Dockery, 2006; Pope III et al., 2002) contributing to premature
66 mortality (Lelieveld et al., 2015).

67 To combat secondary pollution, the European Union established a set of measures
68 focusing on ammonia abatement, similar to the ones introduced by China (Giannakis et al.,
69 2019). These measures aim at reducing ammonia emissions by 6% in 2020, relative to 2005.
70 However, the lack of spatiotemporal measurements of ammonia over Europe makes any
71 assessment of the efficiency of these measures difficult, as only bottom-up methods are used to
72 calculate emission. These methods still show a slight increase ($0.6\% \text{ y}^{-1}$) up to 2018 mostly due
73 to increasing agricultural activities (McDuffie et al., 2020). Such bottom-up approaches rely on
74 uncertain land-use data and emission factors that are not always up to date, thus adding large
75 errors to existing inventories.

76 During the last decade, satellite products have also become available to fill the gaps
77 created by spatially disconnected ground-based measurements. Data from satellite sounders
78 such as the Infrared Atmospheric Sounding Interferometer (IASI) (Van Damme et al., 2017),
79 the Atmospheric Infrared Sounder (AIRS) (Warner et al., 2017), the Cross-track Infrared
80 Sounder (CrIS) (Shephard and Cady-Pereira, 2015), the Tropospheric Emission Spectrometer
81 (TES) (Shephard et al., 2015), and Greenhouse Gases Observing Satellite (GOSAT) (Someya
82 et al., 2020) are publicly available. Most of them have been validated against ground-based
83 observations or complemented with other remote sensing products (Van Damme et al., 2015,
84 2018; Dammers et al., 2016, 2017, 2019; Kharol et al., 2018; Shephard et al., 2020; Whitburn
85 et al., 2016).

86 Accordingly, a few studies on ammonia emission calculations have been recently
87 published relying on 4D-Variational inversion schemes such as (Cao et al., 2022; Zhu et al.,
88 2013) or process based models (Beaudor et al., 2023; Vira et al., 2020). More recently, Sitwell
89 et al. (2022) proposed an inversion scheme for comparison between model profiles and satellite
90 retrievals using hybrid logarithmic and linear observation operator that attempts to choose the
91 best method according to the particular situation. In the present study, we use direct
92 comparisons between the CrIS ammonia retrievals and model profiles using the Least Squares
93 with Adaptive Prior Covariance (LS-APC) algorithm (Tichý et al., 2016), which reduces the
94 number of tuning parameters in the method significantly using variational Bayesian
95 approximation technique. We constrain ammonia emissions over Europe over the 2013–2020
96 period and validate the results against ground-based observations from EMEP (European
97 Monitoring and Evaluation Programme, <https://emep.int/mscw/>) (Torseth et al., 2012).

98 **2 Methods**

99 **2.1 CrIS observations**

100 To constrain ammonia emissions with inverse modelling, satellite measurements were
101 adopted from the Cross-Track Infrared Sounder (CrIS) onboard the NASA Suomi National
102 Polar-orbiting Partnership (S-NPP) satellite, which provides atmospheric soundings with a
103 spectral resolution of 0.625 cm^{-1} (Shephard et al., 2015). CrIS presents improved vertical
104 sensitivity for ammonia closer to the surface due to the low spectral noise in the ammonia
105 spectral region (Zavyalov et al., 2013) and the early afternoon overpass that typically coincides
106 with high thermal contrast, which is optimal for thermal infrared sensitivity. The CrIS Fast
107 Physical Retrieval (CFPR) (Shephard and Cady-Pereira, 2015) retrieves ammonia profiles at

108 14 levels using a physics-based optimal estimation retrieval, which also provides the vertical
109 sensitivity (averaging kernels) and an estimate of the retrieval errors (error covariance matrices)
110 for each measurement. As peak sensitivity typically occurs in the boundary layer between 900
111 and 700 hPa (~ 1 to 3 km) (Shephard et al., 2020) and the surface and total column
112 concentrations are both highly correlated with these boundary layer retrieved levels. The total
113 column random measurement error is estimated in the 10–15% range, with total errors to be
114 ~30% (Shephard et al., 2020). The individual profile retrieval levels show an estimated random
115 measurement error of 10–30 %, with total random errors estimates increasing to 60 to 100%
116 due to the limited vertical resolution (1 degree of freedom of signal for CrIS ammonia). These
117 vertical sensitivity and error output parameters are also useful for using CrIS observations in
118 applications (e.g. data fusion, data assimilation; model-based emission inversions; (Cao et al.,
119 2020; Li et al., 2019)), as a satellite observational operator can be generated in a robust manner.
120 The detection limit of CrIS measurements has been calculated down to 0.3–0.5 ppbv (Shephard
121 et al., 2020). CrIS ammonia has been evaluated against other observations over North America
122 with the Ammonia Monitoring Network (AMoN) (Kharol et al., 2018) and against ground-
123 based Fourier transform infrared (FTIR) spectroscopic observations (Dammers et al., 2017)
124 showing small bias and high correlations.

125 Daily CrIS ammonia (version 1.6.3) was ~~put~~ on a $0.5^\circ \times 0.5^\circ$ grid covering all of Europe
126 (10°W – 50°E , 25°N – 75°N) for the period 2013–2020. Gridding was chosen due to the large
127 number of observations (around 10,000 retrievals per day per vertical level), which made the
128 calculation of source-receptor matrices (SRMs) computationally inefficient. Through ~~gridding~~
129 we limited the number of observation (and thus the number of SRMs to be calculated) to 2000
130 per day per vertical level. Sitwell et al. (2022) showed that the averaging kernels of CrIS
131 ammonia are significant only for the lowest six levels (the upper eight have no influence onto
132 the satellite observations) and therefore we considered only these six vertical levels (~1018–
133 619 hPa). The gridding was performed by averaging the values that fall in each 0.5° resolution
134 grid-cell daily over the 2013 – 2020 period of this study. This type of gridding was selected
135 before previous experience with inverse distance weighting interpolation of satellite
136 observations showed overestimated results of up to 100% (Evangelou et al., 2021). In addition,
137 the quality of gridding with respect to the averaging kernel of CrIS ammonia was evaluated by
138 calculating the standard deviation of the averaged values (Supplementary Figure S 1). The latter
139 shows that the kernel values within each grid-cell were very similar resulting in low gridded
140 standard deviations, and thus low bias caused from the gridding (Supplementary Figure S 1).

Deleted: interpolated

Deleted: to

Deleted: Interpolation

Deleted: interpolation

Formatted: Font: (Default) Times New Roman, Underline colour: Custom Colour (RGB(79,129,189)), Font colour: Auto, Text Outline

Formatted: Font: (Default) Times New Roman, Underline colour: Custom Colour (RGB(79,129,189)), Font colour: Auto, Text Outline

145 **2.2 A priori emissions of ammonia**

146 We used as a priori emissions for ammonia in the inversion algorithm the ones calculated
147 (i) from the most recent version of ECLIPSEv6 (Evaluating the CLimate and Air Quality
148 ImPacts of Short-livEd Pollutants) (Klimont, 2022; Klimont et al., 2017) combined with
149 biomass burning emissions from GFEDv4 (Global Fire Emission Dataset) (Giglio et al., 2013)
150 hereafter “EC6G4”, (ii) a more traditional dataset from ECLIPSEv5, GFEDv4 and GEIA
151 (Global Emissions InitiAtive), hereafter “EGG” (Bouwman et al., 1997; Giglio et al., 2013;
152 Klimont et al., 2017), (iii) emissions calculated from IASI (Infrared Atmospheric Sounding
153 Interferometer) and a 1-dimensional box-model and a modelled lifetime (Evangelou et al.,
154 2021), denoted as “NE” and (iv) from the high resolution dataset of Van Damme et al. (2018)
155 after applying a simple 1-dimensional box-model (Evangelou et al., 2021), hereafter denoted
156 as “VD”. Given the large uncertainty in ammonia emissions illustrated in [Figure 1](#), we
157 calculated the average of these four priors (hereafter “avgENV”) to establish the a priori
158 emissions used in this study.

Deleted: Figure 1

159 **2.3 Lagrangian particle dispersion model for the calculation of source-receptor
160 matrices (SRMs) of ammonia**

161 SRMs were calculated for each $0.5^\circ \times 0.5^\circ$ grid-cell over Europe (10°W – 50°E , 25°N –
162 75°N) using the Lagrangian particle dispersion model FLEXPART version 10.4 (Pisso et al.,
163 2019) adapted to simulate ammonia. The adaptation of the code includes treatment for the loss
164 processes of ammonia adopted from the Eulerian model LMDZ-OR-INCA (horizontal
165 resolution of $2.5^\circ \times 1.3^\circ$ and 39 hybrid vertical levels) that includes all atmospheric processes
166 and a state-of-the-art chemical scheme (Hauglustaine et al., 2004). The model accounts for
167 large-scale advection of tracers (Hourdin and Armengaud, 1999), deep convection (Emanuel,
168 1991), while turbulent mixing in the planetary boundary layer (PBL) is based on a local second-
169 order closure formalism. The model simulates atmospheric transport of natural and
170 anthropogenic aerosols and accounts for emissions, transport (resolved and sub-grid scale), and
171 dry and wet deposition. LMDZ-OR-INCA includes a simple chemical scheme for the ammonia
172 cycle and nitrate particle formation, as well as a state-of-the-art $\text{CH}_4/\text{NO}_x/\text{CO}/\text{NMHC}/\text{O}_3$
173 tropospheric photochemistry (Hauglustaine et al., 2014). To calculate chemical loss of
174 ammonia to PM2.5, after a month of spin-up, global atmospheric transport of ammonia was
175 simulated for 2013–2020 by nudging the winds of the 6-hourly ERA Interim Reanalysis data
176 (Dee et al., 2011) with a relaxation time of 10 days (Hourdin et al., 2006). Using the EGG
177 inventory, we calculated the e-folding lifetime of ammonia in the model, which was adopted in

179 FLEXPART. We refer the reader to (Tichý et al., 2022) for a detailed description of the
180 formalism. Atmospheric linearities of the system and a full validation against ground-based
181 observation are also presented in the same paper.

182 FLEXPART releases computational particles that are tracked backward in time using
183 ERA5 (Hersbach et al., 2020) assimilated meteorological analyses from the European Centre
184 for Medium-Range Weather Forecasts (ECMWF) with 137 vertical layers, a horizontal
185 resolution of $0.5^\circ \times 0.5^\circ$ and one hour temporal resolution. FLEXPART simulates turbulence
186 (Cassiani et al., 2014), unresolved mesoscale motions (Stohl et al., 2005) and includes a deep
187 convection scheme (Forster et al., 2007). SRMs were calculated for 7 days backward in time,
188 at temporal intervals that matched satellite measurements and at spatial resolution of
189 $0.25^\circ \times 0.25^\circ$. This 7-day backward tracking is sufficiently long to include almost all ammonia
190 sources that contribute to surface concentrations at the receptors given a typical atmospheric
191 lifetime of about half a day (Van Damme et al., 2018; Evangelou et al., 2021).

192 **2.4 Inverse modeling algorithm**

193 The inversion method used in the present study relies on optimization of the difference
194 between the CrIS satellite vertical profile observations, denoted as v^{sat} , and retrieved vertical
195 profile, v^{ret} . The latter are obtained by applying an instrument operator applied in logarithm
196 space (Rodgers, 2000) as follows:

$$197 \ln(v^{ret}) = \ln(v^a) + A(\ln(v^{true}) - \ln(v^a)) \quad (1)$$

198 where v^{ret} is the retrieved profile concentration vector, v^a is a priori profile concentration
199 vector used in the satellite retrievals, v^{true} is the hypothetical true profile concentration vector
200 supplied by the model ($v^{true} = v^{mod}$), and A is the averaging kernel matrix (for each
201 $0.5^\circ \times 0.5^\circ$ resolution grid-cell). Eq. (1) provides a useful basis for the calculation of the CrIS
202 retrievals if the retrieval algorithm is performing as designed, i.e., it is unbiased and the root
203 mean square error (RMSE) is within the expected variability. The v^{mod} term can be written as:

$$204 v^{mod} = Mx \quad (2)$$

205 for each grid-cell of the spatial domain, where M is the grid-cell specific SRM calculated with
206 FLEXPART and x is the unknown grid-cell specific emission vector. The SRM matrix M is
207 calculated on circular surroundings around each grid-cell for computational efficiency. We
208 chose circles with a radius of approximately 445 km, equal to 4 degrees, which is shown to be
209 sufficient for reliable emission estimation and low sensitivity has been observed with this
210 choice. Since the vector x is unknown, we replace it by a prior emission x^a (see section 2.2) in
211 the initial step that is gradually refined iteratively based on the satellite observations.

212 The used inversion setup is based on iterative minimization of mismatch between v^{sat}
 213 and v^{ret} updating (iteratively) the emission x such as below:

$$\arg \min_{x^a \rightarrow x} \left\| v^{sat} - v^{ret} \right\|_2^2 \quad (3)$$

215 for each grid-cell of computational domain. The minimization problem is solved in two steps.

216 First, we construct the linear inverse problem for each year where v^{ret} from the given
 217 surroundings, denoted here as S , forms the block-diagonal matrix v_S^{ret} while v^{sat} from the
 218 given surroundings form an associated observation vector v_S^{sat} . This forms the linear inverse
 219 problem:

$$v^{sat} = v_S^{ret} q_S \quad (4)$$

220 where the vector q_S is a vector with coefficients denoting how x^a needs to be refined to obtain
 221 emission estimate vector x . All elements in Eq. 4 are affected by uncertainties originating from
 222 both the observations and model, hence, we employ an inverse algorithm to solve Eq. 4 with
 223 added regularization in the form of prior distributions with specific covariance models. For one
 224 year, 6 vertical profiles, and 4 degrees radius, the size of the the block-diagonal matrix v_S^{ret} is
 225 13896 times 12, hence, the correction coefficient vector q_S contain 12 values corresponding to
 226 each month. We solve Eq. 4 using the least squares with adaptive prior covariance (LS-APC)
 227 algorithm (Tichý et al., 2016). The algorithm is based on variational Bayesian methodology
 228 assuming non-negative solution and favoring solution without abrupt changes and it minimizes
 229 the use of manual tuning (Tichý et al., 2020). The method assumes the data model in the form
 230 of:

$$p(v^{sat}) = N(v_S^{ret} q_S, R) \quad (5)$$

232 where N denotes the multivariate normal distribution and R the covariance matrix assumed in
 233 the form $R = \omega^{-1} I_p$, where I_p is the identity matrix with ones on its diagonal and zeros
 234 elsewhere, and ω is the unknown precision parameter on its diagonal. Following Bayesian
 235 methodology, we assign a prior model to all unknown parameters, i.e. ω and q_S . Their prior
 236 models are selected as:

$$p(\omega) = G(\vartheta_0, \rho_0) \quad (6)$$

$$p(q_S) = tN(0, (LVL)^{-1}, [0, +\infty]) \quad (7)$$

238 where $G(\vartheta_0, \rho_0)$ is the Gamma distribution (conjugate to the normal distribution) with prior
 239 parameters ϑ_0, ρ_0 selected to 10^{-10} achieve non-informative prior. The second term follows
 240 truncated normal distribution with positive support and with specific form of a precision matrix.
 241 We assume the precision matrix in the form of modified Cholesky decomposition which allows
 242 for tractability of estimation of its parameters, matrices V and L . The matrix V is diagonal with
 243

Deleted: with

Deleted: ω

Deleted: s

248 unknown diagonal parameters and the matrix L is lower bidiagonal with ones on the diagonal
249 and unknown parameters on its sub-diagonal, formalized as vectors v and l , respectively.
250 These parameters are estimated within the method, while purpose of vector v is to allow for
251 abrupt changes in q_S , and vector l to favor smooth estimates (see details in Tichý et al. (2016)).
252 All model parameters (ω, q_S, v, l) are estimated using the variational Bayes procedure where
253 we obtain not only point-estimates, but their full posterior distributions.

254 Second, the grid-cell specific coefficient vector q_S is propagated through Eq. 2 into Eq. 1
255 to refine a prior emission x^a and obtain estimated unknown emissions x . To maintain stability
256 of the method, we bound the ratio between prior and posterior emission elements to 0.01 and
257 100, respectively. This choice, motivated by Cao et al. (2020), omits unrealistically small or
258 high emissions, however, the bounds are large enough to allow for new sources, as well as for
259 attenuation of old sources. To introduce these boundaries is necessary since the problem in Eq.
260 1 is ill-conditioned and the propagation through the equation may lead to unrealistic values due
261 to numerical instability. For this reason, these boundaries are needed and the sensitivity to the
262 choice of the prior emission are studied in Section 3.3.

263 Note that CrIS data for some spatiotemporal elements are missing in the dataset. In these
264 cases, we interpolated the missing data following the method proposed by D'Errico (2023),
265 which solves a direct linear system of equations for missing elements, while the extrapolation
266 behavior of the method is linear. Another strategy recently adopted in the literature has been to
267 tackle the missing data using total variation methodology (see details in Fang et al., 2023);
268 however, the method has been limited so far to its use on point-source release, hence we did
269 not use it in this work.

270 **3 Results**

271 **3.1 Emissions of ammonia in Europe (2013–2020)**

272 We analyze the CrIS ammonia satellite observations for Europe (10°W – 50°E , 25°N –
273 75°N) over the 2013–2020 period on monthly basis to derive ammonia emissions using the
274 inverse modelling methodology described in Section 2.4. The inversion algorithm is applied to
275 each year of CrIS observations separately with the use of the avgEENV prior emission. Note
276 that since a diurnal cycle is neither assumed in the Chemistry Transport Model, nor exists in
277 the satellite observations from CrIS, daily emissions of ammonia do not represent a daily mean.

278 The overall resulting spatial distribution of the posterior emissions of ammonia (denoted
279 as posterior_avgEENV) averaged for the whole period are displayed in Figure 2 (top-left). The

Deleted: Figure 2

281 highest emissions occur in Northwestern Europe (including Northern Belgium, the Netherlands
282 and northwestern Germany) and to a smaller extent in the Po Valley (Italy), and the Ebro Valley
283 (Spain). Local maxima are also seen over Pulawy (Poland), South Romania and Kutina
284 (Croatia) due to industrial applications (Clarisse et al., 2019; Van Damme et al., 2018). While
285 ammonia emissions were not calculated high in the Po Valley (8 year average), it has been
286 reported that in Lombardy, about 90% of the ammonia emissions there have been reported to
287 originate from manure management (Lonati and Cernuschi, 2020). The Ebro Valley is
288 characterized by intensive agricultural activities (Lassaletta et al., 2012; Lecina et al., 2010)
289 and the Aragon and Catalonia regions by large pig farms (Van Damme et al., 2022). Finally,
290 both Belgium and The Netherlands are countries in which intensive livestock activity is
291 documented. It consists mostly of dairy cow, beef cattle, pig and chicken farming (Gilbert et
292 al., 2018; Lesschen et al., 2011; Velthof et al., 2012).

293 [Figure 2](#) (top-right) shows the annual posterior emissions discretized monthly for the
294 whole period (solid line) compared to prior ammonia emissions (dashed line), averaged for the
295 domain. Higher emissions than the prior ones were calculated, which is not necessarily
296 attributed to emission increases over Europe, but rather to miscalculation of emissions in the
297 prior bottom-up inventories that were used. A strong seasonal cycle is also observed peaking
298 in the middle of each year (summer) of the study period, but for several of these years, the
299 characteristic bimodal cycle also appears with another peak in spring (Beaudor et al., 2023).

300 To examine more closely the seasonal variability of ammonia emissions in Europe, we
301 present the monthly posterior emissions of ammonia averaged for the whole study period
302 (2013–2020) at the bottom-left panel of [Figure 2](#), together with the prior ones. The total
303 emissions for each month based on the map element size and length of the respective month
304 were averaged for the whole study period. The same was done for each year in the bottom-right
305 panel. The interannual variability over the period between 2013 and 2020, is also apparent in
306 the monthly box and whisker plots of the posterior emissions. In addition, the spatial
307 distribution of monthly ammonia emissions averaged for the eight-year period is given in
308 [Supplementary Figure S 21](#). It appears that ammonia emissions are very low in wintertime (DJF
309 average: 286 Gg) over Europe and increase towards summer (JJA average: 563 Gg), due to
310 temperature dependent volatilization of ammonia (Sutton et al., 2013), with the largest
311 emissions occurring in August (601 Gg). Although a clear peak of fertilization in early spring
312 is missing from the plot, emissions start to increase in early spring to peak in late-summer (Van
313 Damme et al., 2022) corresponding to the start and end of the fertilization periods in Europe
314 (Paulot et al., 2014). Fertilization is tightly regulated in Europe (Ge et al., 2020). It is only

Deleted: Figure 2

Deleted: Figure 2

Deleted: Supplementary Figure S 1

318 allowed from February to mid-September in The Netherlands, while manure application is also
319 only allowed during the same period depending on the type of manure and the type of land (Van
320 Damme et al., 2022). In Belgium, nitrogen fertilizers are only allowed from mid-February to
321 the end of August (Van Damme et al., 2022), so as in Germany (restricted in winter months)
322 (Kuhn, 2017).

323 Finally, [Figure 2](#) (bottom-right) shows the annual posterior emissions for the whole
324 period with the annual total emissions for each year. We observe a significant decrease in
325 ammonia posterior emissions over Europe during the 2013–2020 period. Emissions were
326 estimated as 5431 Gg for 2013 decreasing to 4890 Gg in 2014. A minor increase can be seen
327 in 2015 (5104 Gg), after which a significant decrease of 534 Gg (more than 10%) was estimated,
328 followed by the nearly constant plateau at the levels between 4383 Gg in 2017, 4323 Gg in
329 2019 and finally to 3994 Gg in 2020. The gradual decrease in ammonia emissions over Europe
330 since 2013 is also plotted spatially in [Supplementary Figure S 32](#). It is evident that the
331 restrictions and measures adopted by the European Union to reduce secondary PM formation
332 were successful, as emissions in the hot-spot regions of Belgium, The Netherlands, Germany
333 and Poland declined drastically over time. However, an increase of +4.4% was observed in
334 2015. It has been reported that ammonia emissions increased in 2015 and several European
335 Union Member States, as well as the EU as a whole, exceeded their respective ammonia
336 emission ceilings (EEA, 2017). The increase was reported to be +1.8% and was mainly caused
337 by increased emissions in Germany, Spain, France, and the United Kingdom. This was caused
338 by extensive use of inorganic nitrogen fertilizers (including urea application) in Germany, while
339 increased emissions in Spain were driven by an increase in the consumption of synthetic
340 nitrogen fertilizers and in the number of cattle and pigs (EEA, 2017). It should be mentioned
341 that a false decrease of ammonia in 2020 due to the COVID-19 pandemic is calculated by the
342 current methodology, mainly due to bias created by the decrease of NO_x and SO₂ that are
343 precursor species of the atmospheric acids, with which ammonia reacts (see Tichý et al., 2022).

344 3.2 Country by country ammonia emissions

345 Posterior annual emissions of ammonia for 2013–2020 are plotted for four European
346 regions (Western, Central and Eastern, Northern and Southern Europe), accompanied by
347 relative trends calculated as difference between year 2013 and 2020 divided by the average for
348 the whole period, in the left panel of [Figure 3](#), while the estimated seasonal variation of each
349 region is shown on the right panels averaged over the whole eight-year period. Western Europe
350 includes Ireland, Austria, France, Germany, Belgium, Andorra, Luxembourg, The Netherlands,

Deleted: Figure 2

Deleted: Supplementary Figure S 2

Deleted: Figure 3

354 Switzerland, and United Kingdom; Central and Eastern Europe include Albania, Bosnia and
355 Herzegovina, Bulgaria, Czechia, Croatia, Hungary, Belarus, Slovakia, North Macedonia,
356 Montenegro, Poland, Romania, Moldova, Slovenia, Ukraine, and Serbia; Northern Europe is
357 defined by Denmark, Estonia, Finland, Latvia, Lithuania, Faroe Islands, Norway, and Sweden;
358 finally, Southern Europe includes Cyprus, Greece, Italy, Portugal, Spain.

359 The most significant decreases in ammonia emissions were estimated to be -38% in
360 Central and Eastern Europe and -37% in Western Europe, respectively. Quantitatively, Central
361 and Eastern Europe emissions were estimated to gradually drop from 2190 Gg in 2013 and to
362 1495 Gg in 2020 with a small increase in 2015 (2171 Gg) mainly because Germany, France
363 and the United Kingdom missed their emission targets (EEA, 2017). Western European
364 emissions of ammonia also declined constantly over time from 2041 Gg in 2013 to 1421 Gg in
365 2020. Smaller, yet significant, decreases were calculated over Northern Europe from 398 Gg in
366 2013 to 333 Gg in 2020 (-17%). Finally, Southern Europe exhibited a minor drop between years
367 2013 and 2014 (from 803 Gg in 2013 to 729 Gg in 2014) followed by a small increase until
368 2019 (from 729 to 803 Gg), and then decreased again in 2020 to 743 Gg. Overall, Southern
369 European emissions decreased by -7.62%.

370 The seasonal cycle of ammonia was again characterized by the restrictions applied to the
371 agricultural-related activities by the European Union member states ([Figure 3](#), right panels). As
372 such, emissions in Western, Central and Eastern and Southern Europe were very low in winter
373 and started increasing when fertilization was allowed in early spring, whereas the increasing
374 temperature towards summer increased volatilization and, thus, emissions of ammonia (Van
375 Damme et al., 2022; Ge et al., 2020). Although much less marked than in other European
376 regions due to lower prevailing temperatures and weaker agricultural applications, emissions
377 in Northern Europe show the spring-summer temperature dependence. However, emissions
378 were estimated to be double in winter rather following the cycle of SO₂ (Tang et al., 2020).
379 Emission may increase in Northern Europe in winter because OH and O₃ concentrations are
380 much lower, and the rate of converting SO₂ to sulfate much slower. This means that less sulfate
381 is produced and thus more NH₃ stays in the gas form. [Supplementary Figure S 43](#) shows prior
382 emissions in Western, Central and Eastern, Northern and Southern Europe for EC6G4 and NE
383 emission inventories. Both show the aforementioned increase in emissions during winter in
384 Northeastern Europe. Specifically, the NE emissions that dominate the a priori emissions
385 (avgEENV) as the highest inventory show an extreme winter peak in the north (emissions
386 decline from 105 to 13 Gg). Therefore, there is a very strong dependence of the posterior

Deleted: Figure 3

Deleted: Supplementary Figure S 3

389 seasonality of ammonia in Northern Europe, which may be also influenced by the used prior
390 emissions, see uncertainty analysis in Section 3.3.

391 Country specific emissions of posterior ammonia on a monthly basis (eight-year average
392 emissions) are shown for 20 countries in [Supplementary Figure S 54](#). For countries such as
393 Portugal, Spain, Italy, United Kingdom, The Netherlands, Belgium, Poland, Hungary,
394 Denmark, Belarus and Romania two peaks can be clearly seen in late spring and end of summer.
395 As discussed before, these peaks coincide with the two main fertilization periods in Europe
396 (Paulot et al., 2014). However, it is expected that ammonia abundance is high throughout the
397 entire spring–summer period (e.g., Greece, France, Germany, Czechia, Ukraine and Bulgaria)
398 due to agricultural activity and temperature dependent volatilization (Sutton et al., 2013).
399 Ammonia emissions in Finland, Sweden and Norway are smaller than in the rest of Europe and
400 show a reverse seasonality.

Deleted: Supplementary Figure S 4

401 3.3 Uncertainties in ammonia's posterior emissions

402 For the calculation of uncertainty of the estimated posterior emissions two different
403 approaches were used. The first approach is based on uncertainty arising as a result of the
404 inversion methodology. The standard deviation is calculated from posterior estimate which is
405 in the form of Gaussian distribution such as

$$406 p_{\text{posterior}}(x_i) = N(\mu_i, \sigma_i^2) \quad (8),$$

407 where N denotes normal (Gaussian) distribution and posterior parameters μ_i and σ_i are results
408 of inversion for each element of the spatiotemporal domain. The uncertainty associated with
409 any given spatial element is then a property of Gaussian distribution defined with the square
410 root of summed squared standard deviations:

$$411 \sigma_{\text{location}} = \sqrt{\sum_t \sigma_{\text{location},t}^2} \quad (9)$$

412 Here, $\sigma_{\text{location},t}^2$ denotes the estimated variance of the emissions for given coordinates and time
413 period; we consider uncertainty calculated as 2σ standard deviations, i.e. 95% of the values lay
414 inside the interval with the center in the reported emissions surrounded by the reported
415 uncertainty.

416 The second approach is based on ensemble of the used prior emissions as an input for the
417 inversion. The different ensemble members are built from five prior emissions (see [Figure 1](#))
418 while the uncertainty is calculated as the standard deviation of five resulting posterior
419 emissions.

Deleted: Figure 1

422 2.410 The calculated posterior uncertainty for our spatial domain and studied period
423 (2013–2020) is shown in [Figure 4](#) for Gaussian posterior (left) and for ensemble of prior
424 emissions (right). The uncertainty associated with Gaussian posterior for each year of the study
425 period are depicted in [Supplementary Figure S 65](#). The absolute uncertainty of Gaussian
426 posterior ammonia emissions reaches a maximum of $23.3 \text{ ng m}^{-2} \text{ s}^{-1}$ or about 39% (relative
427 value, calculated based on related maximum of posterior emissions). The uncertainty based on
428 prior ensemble reaches a maximum of $60.2 \text{ ng m}^{-2} \text{ s}^{-1}$ which is equal to about 101% based on
429 related maximum of posterior emissions. In general, the pattern of both posterior uncertainties,
430 Gaussian posterior and prior ensemble respectively, are in agreement in theirs patterns and
431 follow the one of the posterior emissions, with the highest values over (i) Belgium, the
432 Netherlands, and Germany due to livestock, farming, and agricultural activity; (ii) Poland,
433 South Romania and Croatia due to industrial applications; (iii) Catalonia due to pig farming;
434 (iv) West France due to manure application. Nevertheless, the obtained posterior uncertainty
435 remains low, and this depicts the robustness of the methodology used and the calculated
436 posterior emissions of ammonia.

Deleted: Figure 4Figure 4Figure 4

Deleted: Supplementary Figure S 4

437 3.4 Validation of posterior emissions

438 As shown in Eq. 3 (Section 2.4), the inversion algorithm minimizes the distance between
439 the satellite observations (v^{sat}) and the retrieved ammonia concentrations (v^{ret}). The latter is
440 a function of different satellite parameters (e.g., averaging kernel sensitivities) and modelled
441 ammonia concentrations using a prior dataset (v^{mod} or v^{true}) as seen in Eq. 1. The overall
442 result is always propagated to v^{mod} iteratively, each time updating the prior emissions to obtain
443 posterior ammonia. As specified in CrIS guidelines, modelled concentrations (v^{mod}) cannot be
444 directly compared with satellite data (v^{sat}), while comparing v^{sat} with v^{ret} is not a proper
445 validation method, because the comparison is performed for satellite observations that were
446 included in the inversion (dependent observations), and the inversion algorithm has been
447 designed to reduce the v^{sat} - v^{ret} mismatches. This means that the reduction of the posterior
448 retrieved concentration (v^{ret}) mismatches to the observations (v^{sat}) is determined by the
449 weighting that is given to the observations with respect to v^{ret} . A proper validation of the
450 posterior emissions is performed against observations that were not included in the inversion
451 (independent observations).

452 For these reasons, we compare modelled posterior concentrations of ammonia (v^{mod}) at
453 the surface with ground-based observations over Europe from the EMEP (European Monitoring
454 and Evaluation Programme, <https://emep.int/mscw/>) network (Torseth et al., 2012). The

457 measurements are open in public and can be retrieved from <https://ebas.nilu.no>. We used
 458 measurements for all years between 2013 and 2020 from an average of 53 stations with 2928
 459 observations for each station covering all Europe ([Supplementary Figure S 76](#)). The comparison
 460 is plotted for each of the 53 stations separately on a Taylor diagram in [Figure 5](#). For all stations,
 461 the Pearson's correlation coefficient increased for the posterior ammonia (coloured circles)
 462 increased as compared to the prior one (coloured squares) reaching above 0.6 at several stations,
 463 while the normalized root mean square error (nRMSE) and standard deviation were kept below
 464 2 (unitless) and 2 $\mu\text{g m}^{-3}$, respectively, in almost all stations (except SI0008 in Slovenia).

Deleted: Supplementary Figure S 6

Deleted: Figure 5

465 To further show how posterior emissions of ammonia affect modelled concentrations, we
 466 chose six stations (DE0002 in Germany, NO0056 in South Norway, ES0009 in Spain, NL0091
 467 in the Netherlands, HU0002 in Hungary and PL0005 in Poland) from the EMEP network
 468 (highlighted in red in [Supplementary Figure S 76](#)), and we plot prior and posterior
 469 concentrations against ground-based ammonia over time for the whole study period (2013–
 470 2020) in [Supplementary Figure S 87](#). Given the long period of plotting, we average observations
 471 every week and modelled concentrations every month for a more visible representation of the
 472 comparison. To evaluate the comparison, we calculate a number of statistic measures, namely
 473 nRMSE, the normalized mean absolute error (nMAE) and the root mean squared logarithmic
 474 error (RMSLE) as defined below:

$$475 \quad nRMSE = \sqrt{\frac{\sum_{i=1}^n \frac{1}{n} (m_i - o_i)^2}{\frac{1}{n} \sum_{i=1}^n o_i}} \quad nMAE = \frac{\sum_{i=1}^n |m_i - o_i|}{\sum_{i=1}^n o_i}$$

$$476 \quad RMSLE = \sqrt{\frac{1}{n} \sum_{i=1}^n (\log m_i - \log o_i)^2} \quad (11)$$

477 where n is sample size, m and o the individual sample points for model concentrations and
 478 observations of ammonia indexed with i . As one can see in [Supplementary Figure S 87](#), all
 479 statistics were improved in all six stations and posterior concentrations were closer to the
 480 observations. However, individual peaks were in many cases misrepresented in the model.
 481 Whether this is a result of the measurement technique or the fact that local sources cannot be
 482 resolved at the spatiotemporal resolution of CTM and FLEXPART (given the short lifetime of
 483 atmospheric ammonia) needs further research. The best results were obtained at station ES0009
 484 (Spain), where model captures the seasonal variation of the observations during the whole study
 485 period (2013–2020). In all other stations, the seasonality is maintained albeit steep peaks in the
 486 observations are lost.

Deleted: Supplementary Figure S 7

487 [As explained in section 1, ammonia reacts with the available atmospheric acids producing](#)
 488 [secondary aerosols \(Seinfeld and Pandis, 2000\). Therefore, its presence and lifetime in the](#)

494 atmosphere is driven by the atmospheric acids and their precursors, SO₂ and NO₂. Changes in
495 atmospheric levels of these substances have a significant impact on the lifetime of ammonia
496 and its emissions, as highlighted in Tichý et al., (2022). Therefore, it is clear that a wrong
497 representation of trends in modelled SO₂ and NO₂ will lead to systematic biases in the
498 estimated ammonia emission trends. To further demonstrate that the modelling system correctly
499 represents the trends in SO₂ and NO₂, we compare ground-based observations of these two
500 species from the EMEP network (<https://emep.int/mscw/>) against modelled concentrations.

Field Code Changed

501 The comparison is shown in [Supplementary Figure S 9](#) for six random EMEP stations for
502 different years for each of NO₂ and SO₂. The full comparison of the two datasets of
503 observations is plotted in scatterplots of modelled versus measured surface concentrations for
504 NO₂ and SO₂ for all the study period (2013–2020) in [Supplementary Figure S 10](#). A total
505 number of 3,368,660 for SO₂ and 4,252,592 for NO₂ was used in the validation. It is evident
506 that the seasonal variation of the modelled surface concentrations and their magnitude are both
507 represented very well in the model for NO₂ and SO₂. nRMSE was 0.12 – 0.19 for NO₂ and
508 0.09 – 0.25 for SO₂, nMAE 0.39 – 0.94 for NO₂ and 0.48 – 1.2 for SO₂, RMSLE was 0.25 –
509 0.49 for NO₂ and 0.11 – 0.33 for SO₂ in the six stations ([Supplementary Figure S 9](#)). For over
510 4.2 and 3.3 million measurements that were used in this validation of NO₂ and SO₂
511 concentrations for 2013 – 2020 study period, nRMSE values were 0.05 and 0.02, nMAE 0.74
512 and 1.0 and RMSLE 0.50 and 0.40 for NO₂ and SO₂, respectively ([Supplementary Figure S](#)
513 [10](#)).

Formatted: Font: (Default) Times New Roman, Font colour: Auto

Formatted: Indent: First line: 1 cm

Formatted: Font: (Default) Times New Roman, Underline colour: Custom Colour (RGB(79,129,189)), Font colour: Auto, Text Outline

Formatted: Font: (Default) Times New Roman, Font colour: Auto

Formatted: Font: (Default) Times New Roman, Underline colour: Custom Colour (RGB(79,129,189)), Font colour: Auto, Text Outline

514 4 Discussion

515 4.1 Comparison with emissions inferred from satellite observations

516 We compared our posterior estimates with two recently published studies on ammonia
517 emission in Europe (Cao et al., 2022; Luo et al., 2022). Luo et al. (2022) used IASI observations
518 for the period 2008 to 2018 to estimate ammonia emissions in a global domain. Their method
519 was based on updating prior emissions with correction term computed using differences
520 between observed and simulated ammonia columns combined with calculated ammonia
521 lifetimes. The key indicators calculated for the European domain in Luo et al. (2022) are a
522 linear trend for the 2008–2018 period, average annual emissions, and relative trends. Note that
523 we compare our eight-year period with a decade in Luo et al. (2022). The comparison is
524 depicted in [Figure 6](#). Our estimates ([Figure 6](#), left panel) are in good agreement with those
525 calculated by Luo et al. (2022). The linear trend was estimated as -1.27 Tg for the period by

Deleted: Figure 6

Deleted: Figure 6

528 Luo et al. (2022), while our estimate is -1.44 Tg. The spatial distribution of the trend is also
529 given in [Figure 6](#) (left panel). The key decrease is observed mainly in France, Germany, and
530 middle Europe, while the increasing trend is observed mostly in Spain, parts of Italy, and
531 Greece. The average annual ammonia emission for the European domain in Luo et al. (2022)
532 was estimated to be 5.05 Tg while our estimate is 4.63 Tg. Our lower estimate (by
533 approximately 8%) may be attributed to use of more recent period considered in our study, but
534 both methods agree that the trend in Europe is negative. The relative decrease estimated by Luo
535 et al. (2022) is -25.1%, while we calculate -31.02%, which is again in very good agreement.

Deleted: Figure 6

536 Cao et al. (2022) used CrIS observations for the year 2016 in order to estimate ammonia
537 emissions for 25 European Union members (EU25), namely Austria, Belgium, Bulgaria,
538 Croatia, Republic of Cyprus, Czech Republic, Denmark, Estonia, France, Germany, Greece,
539 Hungary, Ireland, Italy, Latvia, Lithuania, Luxembourg, Malta, Netherlands, Poland, Portugal,
540 Romania, Slovakia, Slovenia, and Spain. The method was tested with uni-directional and bi-
541 directional flux schemes. The uni-directional dry deposition scheme assumes only air to surface
542 exchange of ammonia ignoring changes in environmental conditions, while the bi-directional
543 scheme captures dynamics in measured ammonia fluxes. Total estimated ammonia emissions
544 for the EU25 region by the uni-directional scheme (posterior_uni) and the bi-directional scheme
545 (posterior_bi) were reported as 3534 Gg N y⁻¹ and 2850 Gg N y⁻¹, respectively. The
546 posterior_bi estimate is very close to our estimate for EU25 for the year 2016, which is 2712
547 Gg N y⁻¹, while the posterior_uni is approximately 30% higher. A uni-directional dry
548 deposition scheme ignores the impacts of changes in environmental conditions (e.g., soil
549 temperature, soil wetness, soil pH, fertilized condition, and vegetation type) on ammonia
550 emissions from fertilized soil and crops (volatilization), which likely lead to high biases in top-
551 down estimates. Ammonia in LMDz-OR-INCA model, that was used to capture ammonia's
552 losses, resembles a partially bi-directional treatment, where emissions and deposition are both
553 possible at the same time without any use of a compensation point; this may explain the 30%
554 difference.

555 The detailed EU25 emissions for the year 2016 are displayed in [Figure 6](#) (right panel) for
556 posterior_uni (red), posterior_bi (yellow), our post_avgENV (blue), and priors used by Cao
557 et al. (2022) and in our study (dashed red and blue, respectively). As seen from [Figure 6](#), our
558 posterior estimates (post_avgENV) have more similar characteristics with posterior_bi, with
559 monthly difference to be less than factor of 2 positive or negative from Cao et al. (2022). Note
560 that the posterior_uni estimates are always a factor of 3 higher than our posterior estimates for
561 ammonia emissions. The main differences can be observed during February-March and

Deleted: Figure 6

Deleted: Figure 6

565 October-November periods where our estimates are generally lower than those from Cao et al.
566 (2022).

567 Finally, the latest Commission Third Clean Air Outlook published in December 2022
568 (EC, 2022) based on the data reported by the EEA (<https://www.eea.europa.eu/data-and-maps/dashboards/need-directive-data-viewer-7>) concluded (p. 2) that emissions of ammonia in
569 recent years remain worryingly flat or may have increased for some member states. The
570 assessment covers the period we investigated in the present manuscript (2013 – 2020) and
571 shows (for the EU27) a reduction in ammonia emissions of only 2% that is far smaller than that
572 we calculated here (26%). The consistency of our results with those calculated with similar
573 methodologies (Cao et al., 2022; Luo et al., 2022) urges us to believe that such differences in
574 ammonia trends are the result of differences between bottom-up and top-down estimates.

576 4.2 Assessment of ammonia's atmospheric linearities

577 Ammonia is a particularly interesting substance due to its affinity to react with
578 atmospheric acids producing secondary aerosols. In most cases, it is depleted by sulfuric and
579 nitric acids. However, when relative humidity is high and particles are aqueous, sulfate reacts
580 with ammonia and decreases, while the equilibrium vapor pressure of ammonia with nitric acid
581 increases shifting the reaction towards production of free ammonia (Seinfeld and Pandis, 2000).
582 The former reaction is a rare event and lots of prerequisites must be fulfilled to take place.

583 Supplementary Figure S 118a shows the frequency distribution of gain (production of
584 free ammonia – negative numbers) or loss (production of sulphate/nitrate – positive numbers)
585 due to all chemical processes in the inversion domain (10°W–50°E, 25°N–75°N), for the study
586 period (2013 – 2020) and the lowest six sigma-p vertical levels (~1018–619 hPa, see averaging
587 kernels in section 2.1) (Sitwell and Shephard, 2021). The figure shows mostly positive numbers
588 indicating that atmospheric ammonia reacts towards secondary aerosol formation. The spatial
589 distribution of gain/loss of ammonia is shown in Supplementary Figure S 118b. The pixels
590 indicating production of gaseous ammonia are located in marine regions, where we chose to
591 not perform inversions, as they are an order of magnitude lower (Bouwman et al., 1997), thus
592 less significant. No continental pixels showing gain of ammonia were detected, which would
593 cause simulated backwards in time to fail with our Lagrangian model (see next paragraph). Our
594 approximation, although simplistic, provides computational efficiency when simulating SRMs
595 in backward mode using FLEXPART (Pisso et al., 2019).

596 Seibert and Frank (2004) reported that standard Lagrangian particle dispersion models
597 cannot simulate non-linear chemical reactions. First-order chemical reactions, where the

Deleted: In acidic atmospheres where total ammonia (TA=gas, aqueous and solid) is less than twice the total sulfate ([TA]<2[TS]), all the available ammonia is taken up by the aerosol phase. In ammonia-rich environments ([TA]>2[TS]), the excess ammonia reacts with nitric acid forming ammonium nitrate. If RH is too high, ammonium nitrate is aqueous (Seinfeld and Pandis, 2000). As ammonia reacts with sulfate, it neutralizes sulfuric acid decreasing its concentration. Part of the sulfate may be replaced by nitric acid increasing ammonium nitrate content in the aerosol. If RH...

Deleted: the

Deleted: that

Deleted: increases

Deleted: However, production of ammonia

Deleted: in order

Deleted: The latter is illustrated in

Deleted: Supplementary Figure S 8

Deleted: that

Deleted: affecting ammonia

Deleted: to

Deleted:)

Deleted: that were significant in satellite observations (

Deleted: Supplementary Figure S 8

Deleted: were

Deleted: However, all the other processes occurring during the atmospheric transport of trace substances are linear, i.e., advection, diffusion, convective mixing, dry and wet deposition, and radioactive decay. ...

627 reaction rates can be prescribed, are also linear. Non-linear chemistry cannot be calculated
628 because neither the background chemistry is modeled nor is the coupling of the tracked plume
629 (forward or backward) to this background. Technically, the SRM in FLEXPART is calculated
630 for a receptor with a certain mean mixing ratio (χ) and an emitting source ($q_{i,n}$) in a certain
631 discretization of the space (index i) and time (index n), as:

$$\frac{\chi}{q_{i,n}} = \frac{1}{J} \sum_{j=1}^J \Delta t_{i,j,n} \frac{p_{j,n}}{\rho_{i,n}} \quad (12)$$

632 where J is the total number of backward trajectories (particles index j) originating from the
633 position of the receptor χ and ending at a certain discretized time (index n) in certain
634 discretized space position (index i) for a time interval $\Delta t_{i,j,n}$, and where the air density is $\rho_{i,n}$.
635 The further function $p_{j,n}$ ($p_{j,n} \leq 1$) represents the relative (to the initial receptor state) decay
636 of the mass value in the particle in its travel from the receptor to the discretized space time
637 interval (j, n) due to any linear decay process (e.g. deposition, linear chemical decay) for a
638 perfectly conserved scalar $p_{j,n} = 1$. So, for linear decaying species a direct SRM can be
639 calculated explicitly among all relevant receptor points and all positions in space and time. The
640 existence of the SRM (H), linking directly mixing ratios at the receptor points with emissions,
641 is the prerequisite to apply simple inversion algorithms, such as the one in the present study.

642 Inversion of observations to obtain emissions for non-linear chemically reactive species
643 entails the need of a chemistry transport model (CTM) forward (and its adjoint backward) in
644 time from time t_0 to time t_f evolving the full state of the atmosphere, in relation to the
645 emissions and boundary conditions. Subsequently, a cost function is evaluated by an iterative
646 descent gradient method that implies running the adjoint of the forward model (Fortems-
647 Cheiney et al., 2021). Note that an iterative algorithm means that the forward and adjoint
648 models run several times in sequence until the estimated minimum of the cost function is
649 reached.

650 To overcome these complexities, we examine the linearities of our method and show that
651 FLEXPART simulates ammonia efficiently, we evaluate modelled ammonia against ground-
652 based measurements of ammonia from EMEP (<https://emeep.int/mscw/>) in Europe, EANET
653 (East Asia acid deposition NETwork) in Southeastern Asia (<https://www.eanet.asia/>) and
654 AMoN (Ammonia Monitoring Network in the US, AMoN-US; National Air Pollution
655 Surveillance Program (NAPS) sites in Canada) in North America
656 (<http://nadp.slh.wisc.edu/data/AMoN/>). The SRMs for ammonia express the emission
657 sensitivity (in seconds) and yield modelled concentrations at the receptor point when coupled
658 with gridded emissions from EGG (in kg m⁻² s⁻¹, see section 2.2) at the lowest model level

Deleted: -

Deleted: we use

Deleted: to run

Deleted: the

Deleted: network

Deleted: calculated with the backward mode

Deleted: , which

Deleted: s a

Deleted: in

Deleted: (station)

670 (100 m). To check the consistency of the proxy used in the SRMs of ammonia, we also
671 simulated surface concentrations of ammonia with FLEXPART in forward mode using the
672 same emissions (EGG). We have chosen two random ground-based stations from each of the
673 three measuring networks (EMEP, EANET, AMoN) to compare modelled concentrations. For
674 consistency, we also plot the resulting surface concentrations from the LMDz-OR-INCA model
675 ([Supplementary Figure S 129](#)).

Deleted: Here, we used the ECLIPSEv5, GFED4 and GEIA, (EGG) emissions (Bouwman et al., 1997; Giglio et al., 2013; Klimont et al., 2017) to get concentrations. ...

676 Modelled concentrations (forward and backward FLEXPART and the CTM LMDz-OR-
677 INCA) at each station have been averaged to the temporal resolution of the observations.

678 [Supplementary Figure S 1310](#) shows Taylor diagrams of the comparison between FLEXPART
679 simulated concentration in forward and backward mode. Plotting backward versus forward
680 results is a common procedure to infer whether a Lagrangian model produces reasonable results
681 (Eckhardt et al., 2017; Pisso et al., 2019). In general, the forward and backward simulations
682 show very good agreement for the depicted receptor points. For example, ammonia
683 concentration at stations AL99, CA83, and VNA001 ([Supplementary Figure S 129](#)) are
684 simulated similarly, and the mean concentrations are almost identical in the forward and
685 backward modes. However, during some episodes there can be notable differences (e.g., at
686 DE0002R) as seen before (Eckhardt et al., 2017). The main reason is that the backward
687 calculations always give more accurate results as the number of particles released at the receptor
688 is much higher in backward mode than in forward mode; the particles are targeted to a very
689 small location in backward, whereas in forward mode the particles are distributed equally on a
690 global scale and therefore less particles represent each receptor location. Another reason is that
691 transport and especially turbulent processes are parametrized by random motion, which are
692 different for each FLEXPART simulation. Finally, the coordinate system for defining the height
693 layer above ground depends on the meteorological field which is read at the start of the
694 simulation, and this can also cause small deviations. The Taylor diagram for the respective
695 comparison ([Supplementary Figure S 1310](#)) show high Pearson's correlation coefficients
696 (>0.7), low standard deviations (<1 $\mu\text{g N m}^{-3}$) and root means square errors (RMSEs <0.7 μg
697 N m^{-3}).

Deleted: Supplementary Figure S 10

Deleted: Supplementary Figure S 9

Deleted: Supplementary Figure S 10

698 5 Conclusions

699 Today, a large debate takes place about ammonia abatement strategies for Europe, but
700 also for Southeastern Asia, in an effort to reduce secondary formation and, thus, mitigate
701 climate crisis (van Vuuren et al., 2015). These strategies include (a) low nitrogen feed by
702 reducing ammonia emissions at many stages of manure management, from excretion in

710 housing, through storage of manure to application on land, also having positive effects on
711 animal health and indoor climate (Montalvo et al., 2015); (b) low emission livestock housing,
712 which focuses on reducing the surface and time manure is exposed to air by adopting rules and
713 regulations regarding new livestock houses (Poteko et al., 2019); (c) air purification by
714 adopting technologies to clean exhaust air from livestock buildings (Cao et al., 2023) and
715 others. Here we used satellite observations from CrIS and a novel inverse modelling algorithm
716 to study the spatial variability and seasonality of ammonia emissions over Europe. We then
717 evaluated the overall impact of such strategies on the emissions of ammonia for the period
718 2013–2020. The main key messages can be summarized below:

- 719 • The highest emissions over the 2013–2020 study period occur in North Europe (Belgium,
720 the Netherlands and northwestern Germany). At a regional scale, peaks are seen in Western
721 Europe (Poland, South Romania and Croatia) due to industrial activities, in Spain (Ebro
722 Valley, Aragon, Catalonia) due to agricultural activities and farming, in Belgium and The
723 Netherlands due to livestock activity (dairy cow, beef cattle, pig and chicken farming).
- 724 • Ammonia emissions are low in winter (average: 286 Gg) and peak in summer (average:
725 563 Gg), due to temperature dependent volatilization of ammonia, while a notable peak
726 attributed to fertilization can be seen in early spring during some years.
- 727 • Over the 2013–2020 period, European emissions of ammonia decreased from 5431 Gg in
728 2013 to 3994 Gg in 2020 or about -26%. Hence, the restrictions adopted by the European
729 Union members were effective in reducing secondary PM formation.
- 730 • A slight emission increase of +4.4% in 2015 appears for several European Union Member
731 States (Germany, Spain, France, and the United Kingdom) who exceeded the respective
732 ammonia emission targets. Part of the 2020 ammonia decrease might be attributable to the
733 COVID-19 pandemic restrictions.
- 734 • The largest decreases in ammonia emissions were observed in Central and Eastern Europe
735 (-38%, 2190 Gg in 2013 to 1495 Gg in 2020) and in Western Europe (-37%, 2041 Gg in
736 2013 to 1421 Gg in 2020). Smaller decreases were calculated in Northern Europe (-17%,
737 398 Gg in 2013 to 333 Gg in 2020) ~~and~~ Southern Europe (-7.6%, from 803 Gg in 2013 to
738 to 743 Gg in 2020).
- 739 • The maximum calculated absolute uncertainty of Gaussian posterior model was $23.3 \text{ ng m}^{-2} \text{ s}^{-1}$, or about 39% (relative value) and calculated maximum based ensemble of prior
740 emissions was $60.2 \text{ ng m}^{-2} \text{ s}^{-1}$, or about 101% following the spatial distribution of the
741 posterior emissions.

Deleted: and,

744 • Comparison of the concentrations calculated with prior and posterior ammonia emissions
745 against independent (not used in the inversion algorithm) observations showed improved
746 correlation coefficients and low nRMSEs and standard deviations. Looking at timeseries
747 of six randomly selected stations in Europe, we also found that posterior surface
748 concentrations of ammonia were in accordance with the ground-based measurement, also
749 following the observed seasonal trends.

750 • Our results agree very well with those from Luo et al. (2022) (decreasing trend: -1.44
751 versus -1.27 Tg, annual European emissions: 4.63 versus 5.05 Tg) and those from Cao et
752 al. (2022) following their methodology (their posterior _bi estimate for EU25 and year 2016
753 was 2850 Gg N y⁻¹, while we calculate 2712 Gg N y⁻¹).

754 • The relatively low posterior uncertainty and improved statistics in the validation of the
755 posterior surface concentrations denote the robustness of the posterior emissions of
756 ammonia calculated with satellite measurements and our adapted inverse framework.

757

758 **Data availability.** The data generated for the present paper can be downloaded from ZENODO
759 (<https://doi.org/10.5281/zenodo.7646462>). FLEXPARTv10.4 is open access and can be
760 downloaded from <https://www.flexpart.eu/downloads>, while use of ERA5 data is free of
761 charge, worldwide, non-exclusive, royalty-free and perpetual. The inversion algorithm LS-APC
762 is open access from https://www.utia.cas.cz/linear_inversion_methods. CrIS ammonia can be
763 obtained by request to Dr. M. Shephard (Mark.Shephard@ec.gc.ca). EMEP measurements are
764 open in <https://ebas.nilu.no>. FLEXPART SRMs for 2013–2020 can be obtained from the
765 corresponding author upon request.

766
767 **Competing interests.** The authors declare no competing interests.

768
769 **Acknowledgements.** This study was supported by the Research Council of Norway (project
770 ID: 275407, COMBAT – Quantification of Global Ammonia Sources constrained by a
771 Bayesian Inversion Technique). We kindly acknowledge Dr. M. Shephard for providing CrIS
772 ammonia. This work was granted access to the HPC resources of TGCC under the allocation
773 A0130102201 made by GENCI (Grand Equipement National de Calcul Intensif). O. Tichý
774 was supported by the Czech Science Foundation, grant no. GA20-27939S. Special thanks to
775 Dr. M. Cassiani for explaining Lagrangian modelling basics in section 4.2.

Deleted: ndfej

776

777

779 *Author contributions.* O.T. adapted the inversion algorithm, performed the calculations,
780 analyses and wrote the paper. S.E. adapted FLEXPARTv10.4 to model ammonia chemical loss.
781 Y.B. and D.H. set up the CTM model and performed the simulation, the output of which was
782 used as input in FLEXPART. N.E. performed the FLEXPART simulations, contributed to
783 analyses, wrote and coordinated the paper. All authors contributed to the final version of the
784 manuscript.

785
786 **References**

787 Abbatt, J. P. D., Benz, S., Cziczo, D. J., Kanji, Z., Lohmann, U. and Mohler, O.: Solid
788 Ammonium Sulfate Aerosols as Ice Nuclei: A Pathway for Cirrus Cloud Formation,
789 *Science* (80-), 313(September), 1770–1773, 2006.

790 Beaudor, M., Vuichard, N., Lathière, J., Evangelou, N., Damme, M. Van, Clarisse, L.
791 and Hauglustaine, D.: Global agricultural ammonia emissions simulated with the
792 ORCHIDEE land surface model, *Geosci. Model Dev.*, 16, 1053–1081 [online]
793 Available from: <https://doi.org/10.5194/egusphere-2022-626>, 2023.

794 Behera, S. N., Sharma, M., Aneja, V. P. and Balasubramanian, R.: Ammonia in the
795 atmosphere: A review on emission sources, atmospheric chemistry and deposition
796 on terrestrial bodies, *Environ. Sci. Pollut. Res.*, 20(11), 8092–8131,
797 doi:10.1007/s11356-013-2051-9, 2013.

798 Bouwman, A. F., Lee, D. S., Asman, W. A. H., Dentener, F. J., Van Der Hoek, K. W.
799 and Olivier, J. G. J.: A global high-resolution emission inventory for ammonia, *Global
800 Biogeochem. Cycles*, 11(4), 561–587, doi:10.1029/97GB02266, 1997.

801 Cao, H., Henze, D. K., Shephard, M. W., Dammers, E., Cady-Pereira, K., Alvarado,
802 M., Lonsdale, C., Luo, G., Yu, F., Zhu, L., Danielson, C. G. and Edgerton, E. S.:
803 Inverse modeling of NH₃ sources using CrIS remote sensing measurements,
804 *Environ. Res. Lett.*, 15, 104082, doi:10.1088/1748-9326/abb5cc, 2020.

805 Cao, H., Henze, D. K., Zhu, L., Shephard, M. W., Cady-Pereira, K., Dammers, E.,
806 Sitwell, M., Heath, N., Lonsdale, C., Bash, J. O., Miyazaki, K., Flechard, C., Fauvel,
807 Y., Kruit, R. W., Feigenspan, S., Brümmer, C., Schrader, F., Twigg, M. M., Leeson,
808 S., Tang, Y. S., Stephens, A. C. M., Braban, C., Vincent, K., Meier, M., Seitler, E.,
809 Geels, C., Ellermann, T., Sanocka, A. and Capps, S. L.: 4D-Var Inversion of
810 European NH₃ Emissions Using CrIS NH₃ Measurements and GEOS-Chem Adjoint
811 With Bi-Directional and Uni-Directional Flux Schemes, *J. Geophys. Res. Atmos.*,
812 127(9), 1–25, doi:10.1029/2021JD035687, 2022.

813 Cao, T., Zheng, Y., Dong, H., Wang, S., Zhang, Y. and Cong, Q.: A new air cleaning
814 technology to synergistically reduce odor and bioaerosol emissions from livestock
815 houses, *Agric. Ecosyst. Environ.*, 342(October 2022), 108221,
816 doi:10.1016/j.agee.2022.108221, 2023.

817 Cassiani, M., Stohl, A. and Brioude, J.: Lagrangian Stochastic Modelling of
818 Dispersion in the Convective Boundary Layer with Skewed Turbulence Conditions
819 and a Vertical Density Gradient: Formulation and Implementation in the FLEXPART
820 Model, *Boundary-Layer Meteorol.*, 154(3), 367–390, doi:10.1007/s10546-014-9976-
821 5, 2014.

822 Clarisse, L., Van Damme, M., Clerbaux, C. and Coheur, P. F.: Tracking down global
823 NH₃ point sources with wind-adjusted superresolution, *Atmos. Meas. Tech.*, 12(10),
824 5457–5473, doi:10.5194/amt-12-5457-2019, 2019.

825 Crippa, M., Solazzo, E., Huang, G., Guizzardi, D., Koffi, E., Muntean, M., Schieberle,

826 C., Friedrich, R. and Janssens-Maenhout, G.: High resolution temporal profiles in the
827 Emissions Database for Global Atmospheric Research, *Sci. Data*, 7(1), 1–17,
828 doi:10.1038/s41597-020-0462-2, 2020.

829 D'Errico, J.: *Inpaint_nans*, [online] Available from:
830 https://www.mathworks.com/matlabcentral/fileexchange/4551-inpaint_nans, 2023.

831 Van Damme, M., Clarisse, L., Dammers, E., Liu, X., Nowak, J. B., Clerbaux, C.,
832 Flechard, C. R., Galy-Lacaux, C., Xu, W., Neuman, J. A., Tang, Y. S., Sutton, M. A.,
833 Erisman, J. W. and Coheur, P. F.: Towards validation of ammonia (NH₃)
834 measurements from the IASI satellite, *Atmos. Meas. Tech.*, 8(3), 1575–1591,
835 doi:10.5194/amt-8-1575-2015, 2015.

836 Van Damme, M., Whitburn, S., Clarisse, L., Clerbaux, C., Hurtmans, D. and Coheur,
837 P.: Version 2 of the IASI NH 3 neural network retrieval algorithm : near-real-time and
838 reanalysed datasets, *Atmos. Meas. Tech.*, 10, 4905–4914, 2017.

839 Van Damme, M., Clarisse, L., Whitburn, S., Hadji-Lazaro, J., Hurtmans, D., Clerbaux,
840 C. and Coheur, P. F.: Industrial and agricultural ammonia point sources exposed,
841 *Nature*, 564(7734), 99–103, doi:10.1038/s41586-018-0747-1, 2018.

842 Van Damme, M., Clarisse, L., Stavrakou, T., Wichink Kruit, R., Sellekaerts, L., Viatte,
843 C., Clerbaux, C. and Coheur, P. F.: On the weekly cycle of atmospheric ammonia
844 over European agricultural hotspots, *Sci. Rep.*, 12(1), 1–9, doi:10.1038/s41598-022-
845 15836-w, 2022.

846 Dammers, E., Palm, M., Van Damme, M., Vigouroux, C., Smale, D., Conway, S.,
847 Toon, G. C., Jones, N., Nussbaumer, E., Warneke, T., Petri, C., Clarisse, L.,
848 Clerbaux, C., Hermans, C., Lutsch, E., Strong, K., Hannigan, J. W., Nakajima, H.,
849 Morino, I., Herrera, B., Stremme, W., Grutter, M., Schaap, M., Kruit, R. J. W., Notholt,
850 J., Coheur, P. F. and Erisman, J. W.: An evaluation of IASI-NH 3 with ground-based
851 Fourier transform infrared spectroscopy measurements, *Atmos. Chem. Phys.*,
852 16(16), 10351–10368, doi:10.5194/acp-16-10351-2016, 2016.

853 Dammers, E., Shephard, M. W., Palm, M., Cady-pereira, K., Capps, S., Lutsch, E.,
854 Strong, K., Hannigan, J. W., Ortega, I., Toon, G. C., Stremme, W. and Grutter, M.:
855 Validation of the CrIS fast physical NH 3 retrieval with ground-based FTIR, *Atmos.*
856 *Meas. Tech.*, 87, 2645–2667, 2017.

857 Dammers, E., McLinden, C. A., Griffin, D., Shephard, M. W., Van Der Graaf, S.,
858 Lutsch, E., Schaap, M., Gainairu-Matz, Y., Fioletov, V., Van Damme, M., Whitburn,
859 S., Clarisse, L., Cady-Pereira, K., Clerbaux, C., Francois Coheur, P. and Erisman, J.
860 W.: NH₃ emissions from large point sources derived from CrIS and IASI satellite
861 observations, *Atmos. Chem. Phys.*, 19(19), 12261–12293, doi:10.5194/acp-19-
862 12261-2019, 2019.

863 Dee, D. P., Uppala, S. M., Simmons, A. J., Berrisford, P., Poli, P., Kobayashi, S.,
864 Andrae, U., Balmaseda, M. A., Balsamo, G., Bauer, P., Bechtold, P., Beljaars, A. C.
865 M., van de Berg, L., Bidlot, J., Bormann, N., Delsol, C., Dragani, R., Fuentes, M.,
866 Geer, A. J., Haimberger, L., Healy, S. B., Hersbach, H., H??lm, E. V., Isaksen, L.,
867 K??lberg, P., K??hler, M., Matricardi, M., McNally, A. P., Monge-Sanz, B. M.,
868 Morcrette, J. J., Park, B. K., Peubey, C., de Rosnay, P., Tavolato, C., Th??paut, J. N.
869 and Vitart, F.: The ERA-Interim reanalysis: Configuration and performance of the
870 data assimilation system, *Q. J. R. Meteorol. Soc.*, 137(656), 553–597,
871 doi:10.1002/qj.828, 2011.

872 EC: Report from the Commission to the European Parliament, the Council, the
873 European Economic and Social Committee of the regions: The Third Clean Air
874 Outlook, Brussels., 2022.

875 Eckhardt, S., Cassiani, M., Evangelou, N., Sollum, E., Pisso, I. and Stohl, A.:

876 Source-receptor matrix calculation for deposited mass with the Lagrangian particle
877 dispersion model FLEXPART v10.2 in backward mode, *Geosci. Model Dev.*, 10,
878 4605–4618, doi:10.5194/gmd-10-4605-2017, 2017.

879 EEA: European Union emission inventory report 1990 –2015 under the UNECE
880 Convention on Long-range Transboundary Air Pollution. [online] Available from:
881 <https://www.eea.europa.eu/publications/annual-eu-emissions-inventory-report>, 2017.

882 Emanuel, K. A.: A Scheme for Representing Cumulus Convection in Large-Scale
883 Models, *J. Atmos. Sci.*, 48(21), 2313–2329, doi:10.1175/1520-
884 0469(1991)048<2313:ASFRCC>2.0.CO;2, 1991.

885 Erisman, J. W., Bleeker, A., Galloway, J. and Sutton, M. S.: Reduced nitrogen in
886 ecology and the environment, *Environ. Pollut.*, 150(1), 140–149,
887 doi:10.1016/j.envpol.2007.06.033, 2007.

888 Evangelou, N., Balkanski, Y., Eckhardt, S., Cozic, A., Van Damme, M., Coheur, P.-
889 F., Clarisse, L., Shephard, M., Cady-Pereira, K. and Hauglustaine, D.: 10-Year
890 Satellite-Constrained Fluxes of Ammonia Improve Performance of Chemistry
891 Transport Models, *Atmos. Chem. Phys.*, 21, 4431–4451, doi:10.5194/acp-21-4431-
892 2021, 2021.

893 Fang, S., Dong, X., Zhuang, S., Tian, Z., Zhao, Y., Liu, Y., Liu, Y. and Sheng, L.:
894 Inversion of ^{137}Cs emissions following the fukushima accident with adaptive release
895 recovery for temporal absences of observations, *Environ. Pollut.*, 317(September
896 2022), 120814, doi:10.1016/j.envpol.2022.120814, 2023.

897 Forster, C., Stohl, A. and Seibert, P.: Parameterization of convective transport in a
898 Lagrangian particle dispersion model and its evaluation, *J. Appl. Meteorol. Climatol.*,
899 46(4), 403–422, doi:10.1175/JAM2470.1, 2007.

900 Fortems-Cheiney, A., Pison, I., Broquet, G., Dufour, G., Berchet, A., Potier, E.,
901 Coman, A., Siour, G. and Costantino, L.: Variational regional inverse modeling of
902 reactive species emissions with PYVAR-CHIMERE-v2019, *Geosci. Model Dev.*,
903 14(5), 2939–2957, doi:10.5194/gmd-14-2939-2021, 2021.

904 Fowler, D., Muller, J. B. A., Smith, R. I., Dragosits, U., Skiba, U., Sutton, M. A. and
905 Brimblecombe, P.: A CHRONOLOGY OF NITROGEN DEPOSITION IN THE UK,
906 Water, Air, Soil Pollut. Focus, 4, 9–23, 2004.

907 Galloway, J. N., Aber, J. D., Erisman, J. A. N. W., Seitzinger, S. P., Howarth, R. W.,
908 Cowling, E. B. and Cosby, B. J.: The Nitrogen Cascade, *Bioscience*, 53(4), 341–356,
909 doi:10.1641/0006-3568(2003)053[0341:TNC]2.0.CO;2, 2003.

910 Ge, X., Schaap, M., Kranenburg, R., Segers, A., Jan Reinds, G., Kros, H. and De
911 Vries, W.: Modeling atmospheric ammonia using agricultural emissions with
912 improved spatial variability and temporal dynamics, *Atmos. Chem. Phys.*, 20(24),
913 16055–16087, doi:10.5194/acp-20-16055-2020, 2020.

914 Giannakis, E., Kushta, J., Bruggeman, A. and Lelieveld, J.: Costs and benefits of
915 agricultural ammonia emission abatement options for compliance with European air
916 quality regulations, *Environ. Sci. Eur.*, 31(1), doi:10.1186/s12302-019-0275-0, 2019.

917 Giglio, L., Randerson, J. T. and van der Werf, G. R.: Analysis of daily, monthly, and
918 annual burned area using the fourth-generation global fire emissions database
919 (GFED4), *J. Geophys. Res. Biogeosciences*, 118, 317–328, doi:10.1002/jgrg.20042,
920 2013, 2013.

921 Gilbert, M., Nicolas, G., Cinardi, G., Van Boeckel, T. P., Vanwambeke, S. O., Wint,
922 G. R. W. and Robinson, T. P.: Global distribution data for cattle, buffaloes, horses,
923 sheep, goats, pigs, chickens and ducks in 2010, *Sci. Data*, 5, 1–11,
924 doi:10.1038/sdata.2018.227, 2018.

925 Hauglustaine, D. A., Hourdin, F., Jourdain, L., Filiberti, M.-A., Walters, S., Lamarque,

926 J.-F. and Holland, E. A.: Interactive chemistry in the Laboratoire de Meteorologie
927 Dynamique general circulation model: Description and background tropospheric
928 chemistry evaluation, *J. Geophys. Res.*, 109(D04314), doi:10.1029/2003JD003957,
929 2004.

930 Hauglustaine, D. A., Balkanski, Y. and Schulz, M.: A global model simulation of
931 present and future nitrate aerosols and their direct radiative forcing of climate, *Atmos.*
932 *Chem. Phys.*, 14(20), 11031–11063, doi:10.5194/acp-14-11031-2014, 2014.

933 Henze, D. K., Shindell, D. T., Akhtar, F., Spurr, R. J. D., Pinder, R. W., Loughlin, D.,
934 Kopacz, M., Singh, K. and Shim, C.: Spatially Refined Aerosol Direct Radiative
935 Forcing Efficiencies, *Environ. Sci. Technol.*, 46, 9511–9518, doi:10.1021/es301993s,
936 2012.

937 Hersbach, H., Bell, B., Berrisford, P., Hirahara, S., Horányi, A., Muñoz-Sabater, J.,
938 Nicolas, J., Peubey, C., Radu, R., Schepers, D., Simmons, A., Soci, C., Abdalla, S.,
939 Abellan, X., Balsamo, G., Bechtold, P., Biavati, G., Bidlot, J., Bonavita, M., De
940 Chiara, G., Dahlgren, P., Dee, D., Diamantakis, M., Dragani, R., Flemming, J.,
941 Forbes, R., Fuentes, M., Geer, A., Haimberger, L., Healy, S., Hogan, R. J., Hólm, E.,
942 Janisková, M., Keeley, S., Laloyaux, P., Lopez, P., Lupu, C., Radnoti, G., de Rosnay,
943 P., Rozum, I., Vamborg, F., Villaume, S. and Thépaut, J. N.: The ERA5 global
944 reanalysis, *Q. J. R. Meteorol. Soc.*, 146(730), 1999–2049, doi:10.1002/qj.3803, 2020.

945 Hourdin, F. and Armengaud, A.: The Use of Finite-Volume Methods for Atmospheric
946 Advection of Trace Species. Part I: Test of Various Formulations in a General
947 Circulation Model, *Mon. Weather Rev.*, 127(5), 822–837, doi:10.1175/1520-
948 0493(1999)127<0822: TUOFVM>2.0.CO;2, 1999.

949 Hourdin, F., Musat, I., Bony, S., Braconnot, P., Codron, F., Dufresne, J. L., Fairhead,
950 L., Filiberti, M. A., Friedlingstein, P., Grandpeix, J. Y., Krinner, G., LeVan, P., Li, Z. X.
951 and Lott, F.: The LMDZ4 general circulation model: Climate performance and
952 sensitivity to parametrized physics with emphasis on tropical convection, *Clim. Dyn.*,
953 27(7–8), 787–813, doi:10.1007/s00382-006-0158-0, 2006.

954 Kharol, S. K., Shephard, M. W., McLinden, C. A., Zhang, L., Sioris, C. E., O'Brien, J.
955 M., Vet, R., Cady-Pereira, K. E., Hare, E., Siemons, J. and Krotkov, N. A.: Dry
956 Deposition of Reactive Nitrogen From Satellite Observations of Ammonia and
957 Nitrogen Dioxide Over North America, *Geophys. Res. Lett.*, 45(2), 1157–1166,
958 doi:10.1002/2017GL075832, 2018.

959 Klimont, Z.: personal communication, 2022.

960 Klimont, Z., Kupiainen, K., Heyes, C., Purohit, P., Cofala, J., Rafaj, P., Borken-
961 Kleefeld, J. and Schöpp, W.: Global anthropogenic emissions of particulate matter
962 including black carbon, *Atmos. Chem. Phys.*, 17, 8681–8723, doi:10.5194/acp-17- 50
963 8681-2017, 2017.

964 Krupa, S. V.: Effects of atmospheric ammonia (NH₃) on terrestrial vegetation: A
965 review, *Environ. Pollut.*, 124(2), 179–221, doi:10.1016/S0269-7491(02)00434-7,
966 2003.

967 Kuhn, T.: The revision of the German Fertiliser Ordinance in 2017, *Agric. Resour.
968 Econ.*, 2(Discussion Paper), 1–22, 2017.

969 Lassaletta, L., Romero, E., Billen, G., Garnier, J., García-Gómez, H. and Rovira, J.
970 V.: Spatialized N budgets in a large agricultural Mediterranean watershed: High
971 loading and low transfer, *Biogeosciences*, 9(1), 57–70, doi:10.5194/bg-9-57-2012,
972 2012.

973 Lecina, S., Isidoro, D., Playán, E. and Aragüés, R.: Irrigation modernization in Spain:
974 Effects on water quantity and quality-a conceptual approach, *Int. J. Water Resour.
975 Dev.*, 26(2), 265–282, doi:10.1080/07900621003655734, 2010.

976 Lelieveld, J., Evans, J. S., Fnais, M., Giannadaki, D. and Pozzer, A.: The contribution
977 of outdoor air pollution sources to premature mortality on a global scale., *Nature*,
978 525(7569), 367–71, doi:10.1038/nature15371, 2015.

979 Lesschen, J. P., van den Berg, M., Westhoek, H. J., Witzke, H. P. and Oenema, O.:
980 Greenhouse gas emission profiles of European livestock sectors, *Anim. Feed Sci.
981 Technol.*, 166–167, 16–28, doi:10.1016/j.anifeedsci.2011.04.058, 2011.

982 Li, C., Martin, R. V., Shephard, M. W., Pereira, K. C., Cooper, M. J., Kaiser, J., Lee,
983 C. J., Zhang, L. and Henze, D. K.: Assessing the Iterative Finite Difference Mass
984 Balance and 4D - Var Methods to Derive Ammonia Emissions Over North America
985 Using Synthetic Observations, *J. Geophys. Res. Atmos.*, 124, 4222–4236,
986 doi:10.1029/2018JD030183, 2019.

987 Lonati, G. and Cernuschi, S.: Temporal and spatial variability of atmospheric
988 ammonia in the Lombardy region (Northern Italy), *Atmos. Pollut. Res.*, 11(12), 2154–
989 2163, doi:10.1016/j.apr.2020.06.004, 2020.

990 Luo, Z., Zhang, Y., Chen, W., Van Damme, M., Coheur, P.-F. and Clarisse, L.:
991 Estimating global ammonia (NH₃) emissions based on IASI observations from 2008
992 to 2018, *Atmos. Chem. Phys.*, 22(15), 10375–10388, doi:10.5194/acp-22-10375-
993 2022, 2022.

994 Malm, W. C.: Spatial and monthly trends in speciated fine particle concentration in
995 the United States, *J. Geophys. Res.*, 109(D3), D03306, doi:10.1029/2003JD003739,
996 2004.

997 McDuffie, E., Smith, S., O'Rourke, P., Tibrewal, K., Venkataraman, C., Marais, E.,
998 Zheng, B., Crippa, M., Brauer, M. and Martin, R.: A global anthropogenic emission
999 inventory of atmospheric pollutants from sector- and fuel-specific sources (1970–
1000 2017): An application of the Community Emissions Data System (CEDS), *Earth Syst.
1001 Sci. Data Discuss.*, 1–49, doi:10.5194/essd-2020-103, 2020.

1002 Montalvo, G., Pineiro, C., Herrero, M., Bigeriego, M. and Prins, W.: Ammonia
1003 Abatement by Animal Housing Techniques BT - Costs of Ammonia Abatement and
1004 the Climate Co-Benefits, edited by S. Reis, C. Howard, and M. A. Sutton, pp. 53–73,
1005 Springer Netherlands, Dordrecht., 2015.

1006 Paulot, F., Jacob, D. J., Pinder, R. W., Bash, J. O., Travis, K. and Henze, D. K.:
1007 Ammonia emissions in the United States, European Union, and China derived by
1008 high-resolution inversion of ammonium wet deposition data: Interpretation with a new
1009 agricultural emissions inventory (MASAGE-NH₃), *J. Geophys. Res. Atmos.*, 119(7),
1010 4343–4364, doi:10.1002/2013JD021130, 2014.

1011 Pisso, I., Sollum, E., Grythe, H., Kristiansen, N., Cassiani, M., Eckhardt, S., Arnold,
1012 D., Morton, D., Thompson, R. L., Groot Zwaaftink, C. D., Evangelou, N., Sodemann,
1013 H., Haimberger, L., Henne, S., Brunner, D., Burkhardt, J. F., Fouilloux, A., Brioude, J.,
1014 Philipp, A., Seibert, P. and Stohl, A.: The Lagrangian particle dispersion model
1015 FLEXPART version 10.4, *Geosci. Model Dev.*, 12, 4955–4997, doi:10.5194/gmd-12-
1016 4955-2019, 2019.

1017 Pope, C. A. and Dockery, D. W.: Health effects of fine particulate air pollution: Lines
1018 that connect, *J. Air Waste Manag. Assoc.*, 56(6), 709–742,
1019 doi:10.1080/10473289.2006.10464485, 2006.

1020 Pope III, C. A., Burnett, R. T., Thun, M. J., Calle, E. E., Krewski, D. and Thurston, G.
1021 D.: Lung Cancer, Cardiopulmonary Mortality, and Long-term Exposure to Fine
1022 Particulate Air Pollution, *J. Am. Med. Assoc.*, 287(9), 1132–1141,
1023 doi:10.1001/jama.287.9.1132, 2002.

1024 Poteko, J., Zähner, M. and Schrade, S.: Effects of housing system, floor type and
1025 temperature on ammonia and methane emissions from dairy farming: A meta-

1026 analysis, *Biosyst. Eng.*, 182, 16–28, doi:10.1016/j.biosystemseng.2019.03.012, 2019.

1027 Rodgers, C. D.: *Inverse methods for atmospheres: Theory and practice.*, 2000.

1028 Seibert, P. and Frank, A.: Source-receptor matrix calculation with a Lagrangian

1029 particle dispersion model in backward mode, *Atmos. Chem. Phys.*, 4(1), 51–63,

1030 doi:10.5194/acp-4-51-2004, 2004.

1031 Seinfeld, J. H. and Pandis, S. N.: *Atmospheric Chemistry and Physics. From Air*

1032 *Pollution to Climate Change*, 2nd ed., John Wiley & Sons, NY., 2000.

1033 Shephard, M. W. and Cady-Pereira, K. E.: Cross-track Infrared Sounder (CrIS)

1034 satellite observations of tropospheric ammonia, *Atmos. Meas. Tech.*, 8(3), 1323–

1035 1336, doi:10.5194/amt-8-1323-2015, 2015.

1036 Shephard, M. W., McLinden, C. A., Cady-Pereira, K. E., Luo, M., Moussa, S. G.,

1037 Leithead, A., Liggio, J., Staebler, R. M., Akingunola, A., Makar, P., Lehr, P., Zhang,

1038 J., Henze, D. K., Millet, D. B., Bash, J. O., Zhu, L., Wells, K. C., Capps, S. L.,

1039 Chaliyakunnel, S., Gordon, M., Hayden, K., Brook, J. R., Wolde, M. and Li, S. M.:

1040 Tropospheric Emission Spectrometer (TES) satellite observations of ammonia,

1041 methanol, formic acid, and carbon monoxide over the Canadian oil sands: Validation

1042 and model evaluation, *Atmos. Meas. Tech.*, 8(12), 5189–5211, doi:10.5194/amt-8-

1043 5189-2015, 2015.

1044 Shephard, M. W., Dammers, E., E. Cady-Pereira, K., K. Kharol, S., Thompson, J.,

1045 Gainariu-Matz, Y., Zhang, J., A. McLinden, C., Kovachik, A., Moran, M., Bittman, S.,

1046 E. Sioris, C., Griffin, D., J. Alvarado, M., Lonsdale, C., Savic-Jovcic, V. and Zheng,

1047 Q.: Ammonia measurements from space with the Cross-track Infrared Sounder:

1048 Characteristics and applications, *Atmos. Chem. Phys.*, 20(4), 2277–2302,

1049 doi:10.5194/acp-20-2277-2020, 2020.

1050 Sigurdarson, J. J., Svane, S. and Karring, H.: The molecular processes of urea

1051 hydrolysis in relation to ammonia emissions from agriculture, *Rev. Environ. Sci.*

1052 *Biotechnol.*, 17(2), 241–258, doi:10.1007/s11157-018-9466-1, 2018.

1053 Sitwell, M. and Shephard, M.: An Ensemble-Variational Inversion System for the

1054 Estimation of Ammonia Emissions using CrIS Satellite Ammonia Retrievals, , (x),

1055 2021.

1056 Sitwell, M., Shephard, M. W., Rochon, Y., Cady-Pereira, K. and Dammers, E.: An

1057 ensemble-variational inversion system for the estimation of ammonia emissions

1058 using CrIS satellite ammonia retrievals, *Atmos. Chem. Phys.*, 22(10), 6595–6624,

1059 doi:10.5194/acp-22-6595-2022, 2022.

1060 Someya, Y., Imasu, R., Shiomi, K. and Saitoh, N.: Atmospheric ammonia retrieval

1061 from the TANSO-FTS / GOSAT thermal infrared sounder, *Atmos. Meas. Tech.*, 13,

1062 309–321, 2020.

1063 Stevens, C. J., Dupr, C., Dorland, E., Gaudnik, C., Gowing, D. J. G., Bleeker, A.,

1064 Diekmann, M., Alard, D., Bobbink, R., Fowler, D., Corcket, E., Mountford, J. O.,

1065 Vandvik, V., Aarrestad, P. A., Muller, S. and Dise, N. B.: Nitrogen deposition

1066 threatens species richness of grasslands across Europe, *Environ. Pollut.*, 158(9),

1067 2940–2945, doi:10.1016/j.envpol.2010.06.006, 2010.

1068 Stohl, A., Forster, C., Frank, A., Seibert, P. and Wotawa, G.: Technical note: The

1069 Lagrangian particle dispersion model FLEXPART version 6.2, *Atmos. Chem. Phys.*,

1070 5(9), 2461–2474, doi:10.5194/acp-5-2461-2005, 2005.

1071 Sutton, M. A., Erisman, J. W., Dentener, F. and Möller, D.: Ammonia in the

1072 environment: From ancient times to the present, *Environ. Pollut.*, 156(3), 583–604,

1073 doi:10.1016/j.envpol.2008.03.013, 2008.

1074 Sutton, M. A., Reis, S., Riddick, S. N., Dragosits, U., Nemitz, E., Theobald, M. R.,

1075 Tang, Y. S., Braban, C. F., Vieno, M., Dore, A. J., Mitchell, R. F., Wanless, S., Daunt,

1076 F., Fowler, D., Blackall, T. D., Milford, C., Flechard, C. R., Loubet, B., Massad, R.,
1077 Cellier, P., Personne, E., Coheur, P. F., Clarisse, L., Damme, M. Van, Ngadi, Y.,
1078 Clerbaux, C., Skjøth, C. A., Geels, C., Hertel, O., Kruit, R. J. W., Pinder, R. W., Bash,
1079 J. O., Walker, J. T., Simpson, D., Horvath, L., Misselbrook, T. H., Bleeker, A.,
1080 Dentener, F. and Vries, W. de: Towards a climate-dependent paradigm of ammonia
1081 emission and deposition, *Philos. Trans. R. Soc. B Biol. Sci.*, 368(1621), 20130166–
1082 20130166, doi:10.1098/rstb.2013.0166, 2013.
1083 Tang, Y. S., Flechard, C., Dämmgen, U., Vidic, S., Djuricic, V., Mitosinkova, M.,
1084 Uggerud, H., Sanz, M., Simmons, I., Dragosits, U., Nemitz, E., Twigg, M., van Dijk,
1085 N., Fauvel, Y., Sanz-Sanchez, F., Ferm, M., Perrino, C., Catrambone, M., Leaver, D.,
1086 Braban, C., Cape, J. N., Heal, M. and Sutton, M.: Pan-European rural atmospheric
1087 monitoring network shows dominance of NH₃; gas and
1088 NH₄; aerosol in inorganic pollution
1089 load, *Atmos. Chem. Phys. Discuss.*, 1–61, 2020.
1090 Tichý, O., Šmídl, V., Hofman, R. and Stohl, A.: LS-APC v1.0: A tuning-free method
1091 for the linear inverse problem and its application to source-Term determination,
1092 *Geosci. Model Dev.*, 9(11), 4297–4311, doi:10.5194/gmd-9-4297-2016, 2016.
1093 Tichý, O., Ulrych, L., Šmídl, V., Evangelou, N. and Stohl, A.: On the tuning of
1094 atmospheric inverse methods: Comparisons with the European Tracer Experiment
1095 (ETEX) and Chernobyl datasets using the atmospheric transport model FLEXPART,
1096 *Geosci. Model Dev.*, 13(12), 5917–5934, doi:10.5194/gmd-13-5917-2020, 2020.
1097 Tichý, O., Otervik, M. S., Eckhardt, S., Balkanski, Y., Hauglustaine, D. and
1098 Evangelou, N.: NH₃ levels over Europe during COVID-19 were modulated by
1099 changes in atmospheric chemistry, *npj Clim. Atmos. Sci.*, in review, 1–13,
1100 doi:10.21203/rs.3.rs-1930069/v1, 2022.
1101 Torseth, K., Aas, W., Breivik, K., Fjeraa, A. M., Fiebig, M., Hjellbrekke, A. G., Lund
1102 Myhre, C., Solberg, S. and Yttri, K. E.: Introduction to the European Monitoring and
1103 Evaluation Programme (EMEP) and observed atmospheric composition change
1104 during 1972–2009, *Atmos. Chem. Phys.*, 12(12), 5447–5481, doi:10.5194/acp-12-
1105 5447-2012, 2012.
1106 Tsimpidi, A. P., Karydis, V. A. and Pandis, S. N.: Response of inorganic fine
1107 particulate matter to emission changes of sulfur dioxide and ammonia: The Eastern
1108 United States as a case study, *J. Air Waste Manag. Assoc.*, 57(12), 1489–1498,
1109 doi:10.3155/1047-3289.57.12.1489, 2007.
1110 Velthof, G. L., van Bruggen, C., Groenestein, C. M., de Haan, B. J., Hoogeveen, M.
1111 W. and Huijsmans, J. F. M.: A model for inventory of ammonia emissions from
1112 agriculture in the Netherlands, *Atmos. Environ.*, 46, 248–255,
1113 doi:10.1016/j.atmosenv.2011.09.075, 2012.
1114 Vira, J., Hess, P., Melkonian, J. and Wieder, W. R.: An improved mechanistic model
1115 for ammonia volatilization in Earth system models: Flow of Agricultural Nitrogen
1116 version 2 (FANv2), *Geosci. Model Dev.*, 13(9), 4459–4490, doi:10.5194/gmd-13-
1117 4459-2020, 2020.
1118 van Vuuren, A. M., Pineiro, C., van der Hoek, K. W. and Oenema, O.: Economics of
1119 Low Nitrogen Feeding Strategies BT - Costs of Ammonia Abatement and the
1120 Climate Co-Benefits, edited by S. Reis, C. Howard, and M. A. Sutton, pp. 35–51,
1121 Springer Netherlands, Dordrecht., 2015.
1122 Warner, J. X., Dickerson, R. R., Wei, Z., Strow, L. L., Wang, Y. and Liang, Q.:
1123 Increased atmospheric ammonia over the world's major agricultural areas detected
1124 from space, *Geophys. Res. Lett.*, 44, 1–10, doi:10.1002/2016GL072305, 2017.
1125 Whitburn, S., Van Damme, M., Clarisse, L., Bauduin, S., Heald, C. L., Hadji-Lazaro,

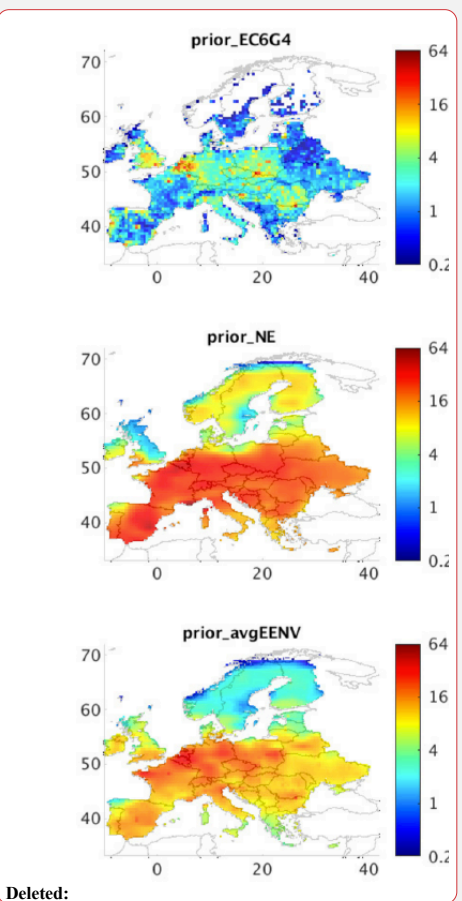
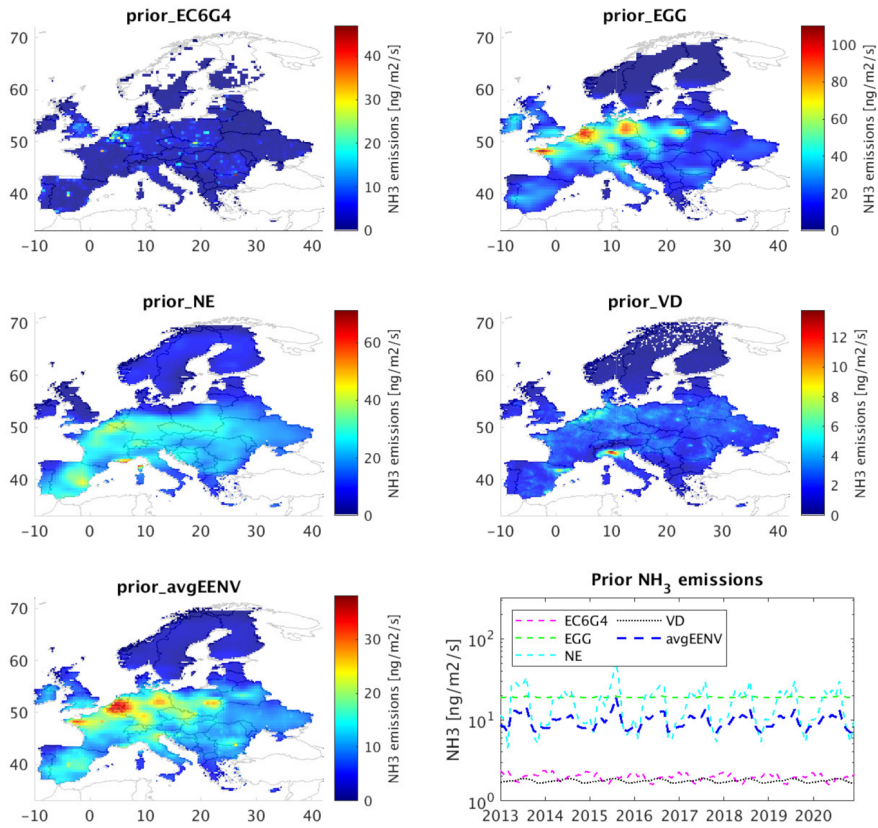
1126 J., Hurtmans, D., Zondlo, M. A., Clerbaux, C. and Coheur, P. F.: A flexible and robust
1127 neural network IASI-NH₃ retrieval algorithm, *J. Geophys. Res.*, 121(11), 6581–6599,
1128 doi:10.1002/2016JD024828, 2016.

1129 Zavyalov, V., Esplin, M., Scott, D., Esplin, B., Bingham, G., Hoffman, E., Lietzke, C.,
1130 Predina, J., Frain, R., Suwinski, L., Han, Y., Major, C., Graham, B. and Phillips, L.:
1131 Noise performance of the CrIS instrument, , 118, 108–120,
1132 doi:10.1002/2013JD020457, 2013.

1133 Zhu, L., Henze, D. K., Cady-Pereira, K. E., Shephard, M. W., Luo, M., Pinder, R. W.,
1134 Bash, J. O. and Jeong, G. R.: Constraining U.S. ammonia emissions using TES
1135 remote sensing observations and the GEOS-Chem adjoint model, *J. Geophys. Res.*
1136 *Atmos.*, 118(8), 3355–3368, doi:10.1002/jgrd.50166, 2013.

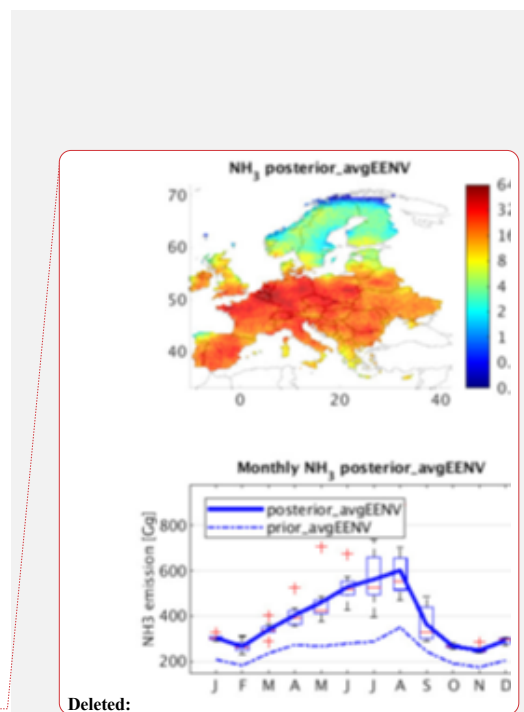
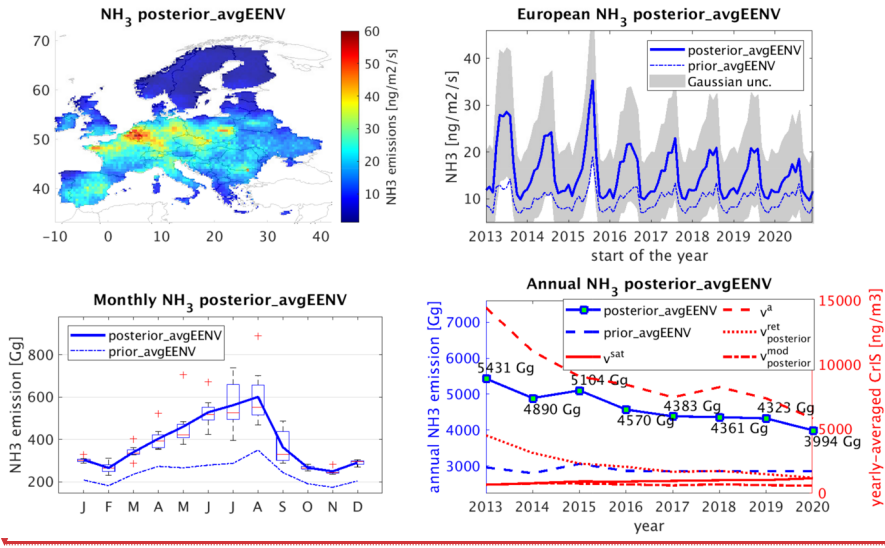
1137

1138

1139 **FIGURES & LEGENDS**

1141 **Figure 1.** Four ammonia prior emissions (EC6G4, EGG, NE, VD) are displayed in the first two
1142 rows. The combined prior (avgEENV) is displayed in the bottom left. The temporal variability
1143 of all five prior emissions is given in bottom right.

1144



Deleted:

Deleted: (

Deleted:) and annually average (bottom-right) estimates are also plotted...

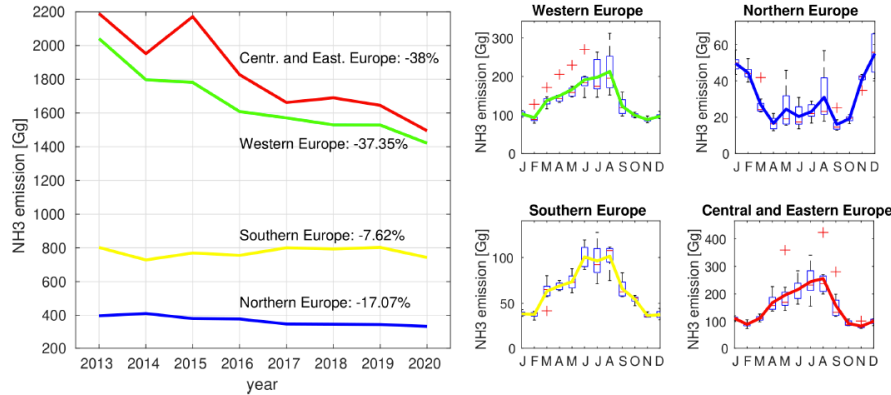
Formatted: Font: 12 pt

Formatted: Font: 12 pt

Formatted: Font: Not Bold

Formatted: Font: Not Bold

Formatted: Font: Not Bold



1164

1165 **Figure 3.** Left: Annual posterior emissions of ammonia in Southern (yellow), Western (green),
1166 Northern (blue), and Central and Eastern (red) Europe. Right: Monthly average posterior
1167 emissions of ammonia accompanied by box plots, where the red line indicates the median, the
1168 bottom and top edges of the box indicate the 25th and 75th percentiles, respectively, and the
1169 whiskers extend to the most extreme data points (not considered outliers), which are represented
1170 using red crosses.

1171

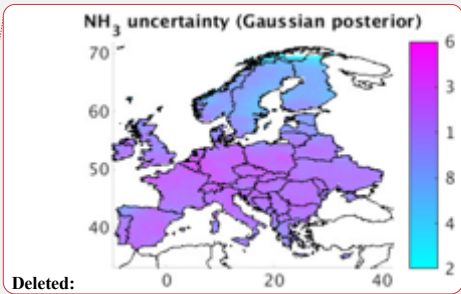
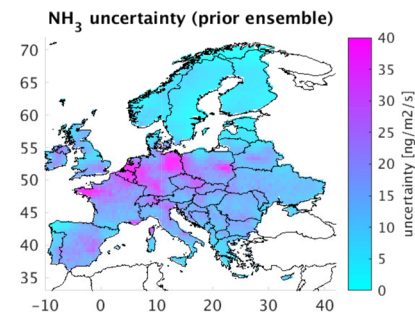
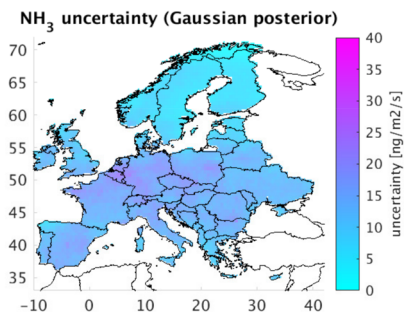
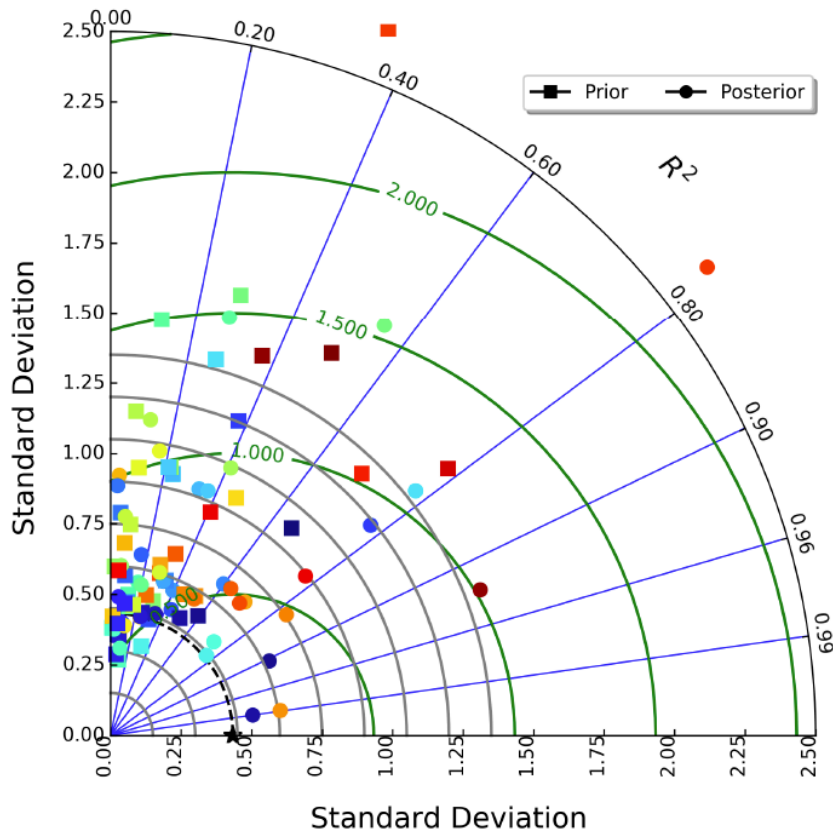


Figure 4. Absolute uncertainty of posterior emissions of ammonia calculated as 2σ (left panel) and from a member ensemble (right panel) comprising posterior emissions calculated with five different priors (Figure 1) averaged for the whole study period 2013–2020.

Comparison with EMEP observations

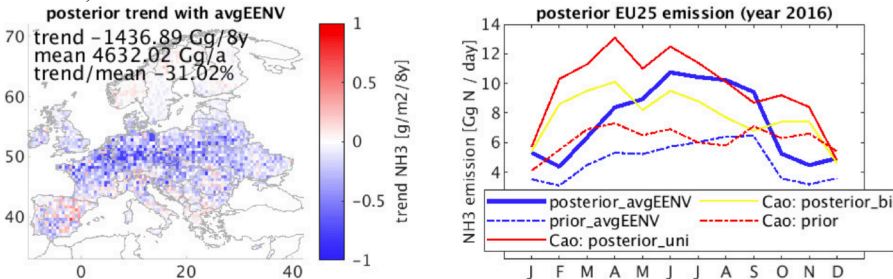
★ Ref.	DK0003	ES0009	GB0013	NL0091	SE0011	DE0009	GB1055
AM0001	DK0008	FI0009	GB0014	NO0002	SE0012	ES0014	HU0003
BE0014	DK0012	FI0017	GB0048	NO0015	SE0014	LV0010	SE0020
CH0002	DK0031	FI0022	GB0054	NO0039	SK0006	NL0007	CH0053
CH0005	ES0001	FI0036	GE0001	NO0056	DE0001	SI0008	FI0050
DE0002	ES0007	FI0037	HU0002	PL0005	DE0003	FI0018	SE0022
DE0007	ES0008	GB0006	IT0001	SE0005	DE0008		



1179

1180 **Figure 5.** Modelled concentrations of ammonia with prior and posterior emissions against
1181 ground-based observations from 53 EMEP stations for 2013–2020 presented in a Taylor
1182 diagram. The diagram shows the Pearson's correlation coefficient (gauging similarity in pattern
1183 between the modelled and observed concentrations) that is related to the azimuthal angle (blue
1184 contours); the standard deviation of modelled concentrations of ammonia is proportional to the
1185 radial distance from the origin (black contours) and the centered normalized RMSE of modelled
1186 concentrations is proportional to the distance from the reference standard deviation (green

1187 contours).



1188

1189 **Figure 6.** Left: spatial distribution of ammonia emission trends computed for the studied period
1190 2013–2020 in the same way as in (Luo et al., 2022), where also trend, mean, and trend/mean
1191 are defined/computed in the same way. Right: comparison of ammonia emissions from the
1192 EU25 countries for the year 2016 from our posterior calculations (posterior_avgENV, blue)
1193 and results from Cao et al. (2022) (posterior_uni in red and posterior_bi, in yellow).

1194